

A misaligned protostellar disk fed by gas streamers in a barred spiral-like massive dense core

Xiaofeng Mai^{1,2,3*}, Tie Liu^{1,4*}, Xunchuan Liu^{1,5}, Bo Zhang^{1,4}, Paul F. Goldsmith⁶, Neal J. Evans II⁷, Qizhou Zhang⁸, Kee-Tae Kim^{9,10}, Dongting Yang¹¹, Mika Juvela³, Fengwei Xu^{12,13,14}, Wenyu Jiao¹, Hongli Liu¹¹, Patricio Sanhueza¹⁵, Guido Garay^{16,17}, Xi Chen¹⁸, Shengli Qin¹¹, Jakobus M. Vorster³, Anandmayee Tej¹⁹, Zhiyuan Ren²⁰, Sami Dib²¹, Shanghuo Li^{22,23}, Qiuyi Luo^{1,2,24}, Jihye Hwang^{25,26}, Prasanta Gorai^{27,28}, Ariful Hoque²⁹, Yichen Zhang³⁰, Jeong-Eun Lee^{31,32}, Siju Zhang¹⁶, Emma Mannfors³, Devika Tharakkal³, Lokesh Dewangan³³, Leonardo Bronfman¹⁶, Pablo García^{17,34}, Xindi Tang³⁵, Swagat R. Das¹⁶, Gang Wu³⁵, Chang-Won Lee⁹, James O. Chibueze^{36,37,38}, Yankun Zhang¹, Qilao Gu¹, Ken'ichi Tatematsu^{24,39}, Guangli Wang¹, Lei Zhu¹⁷, and Zhiqiang Shen^{1,4}

¹Shanghai Astronomical Observatory, Chinese Academy of Sciences, Shanghai 200030, PR China; maixf@shao.ac.cn; liutie@shao.ac.cn;

²School of Astronomy and Space Sciences, University of Chinese Academy of Sciences, No. 19A Yuquan Road, Beijing 100049, People's Republic of China

³Department of Physics, PO Box 64, 00014, University of Helsinki, Finland

⁴State Key Laboratory of Radio Astronomy and Technology, A20 Datun Road, Chaoyang District, Beijing, 100101, P. R. China

⁵Leiden Observatory, Leiden University, P.O. Box 9513, 2300RA Leiden, The Netherlands

⁶Jet Propulsion Laboratory, California Institute of Technology, 4800 Oak Grove Drive, Pasadena, CA 91109, USA

⁷Department of Astronomy, The University of Texas at Austin, 2515 Speedway, Austin, TX 78712, USA

⁸Center for Astrophysics — Harvard & Smithsonian, 60 Garden Street, Cambridge, MA 02138, USA

⁹Korea Astronomy and Space Science Institute (KASI), 776 Daedeokdae-ro, Yuseong-gu, Daejeon 34055, Republic of Korea

¹⁰University of Science and Technology, Korea (UST), 217 Gajeong-ro, Yuseong-gu, Daejeon 34113, Republic of Korea

¹¹School of Physics and Astronomy, Yunnan University, Kunming, 650091, People's Republic of China

¹²Department of Astronomy, Peking University, 100871 Beijing, People's Republic of China

¹³Kavli Institute for Astronomy and Astrophysics, Peking University, 5 Yiheyuan Road, Haidian District, Beijing 100871, People's Republic of China

¹⁴I. Physikalisches Institut, Universität zu Köln, Zùlpicher Straße 77, 50937 Cologne, Germany

¹⁵Department of Astronomy, School of Science, The University of Tokyo, 7-3-1 Hongo, Bunkyo, Tokyo 113-0033, Japan

¹⁶Departamento de Astronomía, Universidad de Chile, Camino el Observatorio 1515, Las Condes, Santiago, Chile

¹⁷Chinese Academy of Sciences South America Center for Astronomy, National Astronomical Observatories, Chinese Academy of Sciences, Beijing 100101, China

¹⁸Center for Astrophysics, Guangzhou University, Guangzhou 510006, People's Republic of China

¹⁹Indian Institute of Space Science and Technology, Thiruvananthapuram 695 547, Kerala, India

²⁰National Astronomical Observatories, CAS, Beijing, China

²¹Max-Planck-Institut für Astronomie, Königstuhl 17, D-69117 Heidelberg, Germany

²²School of Astronomy and Space Science, Nanjing University, 163 Xianlin Avenue, Nanjing 210023, People's Republic of China

²³Key Laboratory of Modern Astronomy and Astrophysics (Nanjing University), Ministry of Education, Nanjing 210023, People's Republic of China

²⁴National Astronomical Observatory of Japan, National Institutes of Natural Sciences, 2-21-1 Osawa, Mitaka, Tokyo 181-8588, Japan

²⁵Institute for Advanced Study, Kyushu University, 774 Motooka Nishi-ku Fukuoka, Japan

²⁶Department of Earth and Planetary Sciences, Faculty of Science, Kyushu University, Nishi-ku, Fukuoka 819-0395, Japan

²⁷Roseland Centre for Solar Physics, University of Oslo, PO Box 1029 Blindern, 0315, Oslo, Norway

²⁸Institute of Theoretical Astrophysics, University of Oslo, PO Box 1029 Blindern, 0315, Oslo, Norway

²⁹S. N. Bose National Centre for Basic Sciences, Block-JD, Sector-III, Salt Lake City, Kolkata 700106, India

³⁰Department of Astronomy, Shanghai Jiao Tong University, 800 Dongchuan Rd., Minhang, Shanghai 200240, People's Republic of China

³¹Department of Physics and Astronomy, Seoul National University, 1 Gwanak-ro, Gwanak-gu, Seoul 08826, Republic of Korea

³²SNU Astronomy Research Center, Seoul National University, 1 Gwanak-ro, Gwanak-gu, Seoul 08826, Republic of Korea

³³Physical Research Laboratory, Navrangpura, Ahmedabad 380 009, India

³⁴Instituto de Astronomía, Universidad Católica del Norte, Av. Angamos 0610, Antofagasta, Chile

³⁵Xinjiang Astronomical Observatory, Chinese Academy of Sciences (CAS), Urumqi 830011, People's Republic of China

³⁶Centre for Space Research, North-West University, Potchefstroom 2520, South Africa

³⁷Department of Mathematical Sciences, University of South Africa, Cnr Christian de Wet Rd and Pioneer Avenue, Florida Park, 1709, Roodepoort, South Africa

³⁸Department of Physics and Astronomy, Faculty of Physical Sciences, University of Nigeria, Carver Building, 1 University Road, Nsukka 410001, Nigeria

³⁹Astronomical Science Program, Graduate Institute for Advanced Studies, SOKENDAI, 2-21-1 Osawa, Mitaka, Tokyo 181-8588, Japan

September 22, 2025

High-mass stars, born in massive dense cores (MDCs), profoundly impact the cosmic ecosystem through feedback processes and metal enrichment, yet little is known about how MDCs assemble and transfer mass across scales to form high-mass young stellar objects (HMYSOs). Using multi-scale (40–2500 au) observations of an MDC hosting an HMYSO, we identify a coherent dynamical structure analogous to barred spiral galaxies: three $\sim 20,000$ au spiral arms feed a $\sim 7,500$ au central bar, which channels gas to a $\sim 2,000$ au pseudodisk. Further accretion proceeds through the inner structures, including a Keplerian disk and an inner disk (~ 100 au), which are thought to be driving a collimated bipolar outflow. This is the first time that these multi-scale structures (spiral arms, bar, streamers, envelope, disk, and outflow) have been simultaneously observed as a physically coherent structure within an MDC. Our discovery suggests that well-organized hierarchical structures play a crucial role during the gas accretion and angular momentum build-up of a massive disk.

Introduction

High-mass stars are known to form within clustered environment (*1–4* and the references therein). Unlike their low-mass solar-type siblings that form from the monolithic collapse of a well-defined pre-stellar core (*5–7*), the formation of the massive stars relies on multi-scale accretion from much larger ($\sim 0.1–1$ pc) gas reservoirs, called massive dense cores (MDCs) (*3*). The MDCs themselves may also continuously accrete gas from their natal clouds through larger-scale ($\sim 1–10$ pc) hierarchical gas structures such as filament-hub systems (*8–10*). However, the formation of gas structures within MDCs and their roles in protostellar mass growth remains elusive. In addition, due to the low number statistics (*11–16*), it is still under debate whether stable disks widely exist in the surroundings of HMYSOs. Therefore, understanding how mass is assembled and transferred across scales to massive disks is essential to constraining the physical mechanisms that govern high-mass star formation, including angular momentum regulation and disk evolution.

At a distance of 1.25 kpc from the Sun (*17*), MDC IRAS 18134-1942 (G11.497-1.485, hereafter I18134) is a massive cloud core containing a UC HII region (*18*), with a gas mass of $238 M_{\odot}$ enclosed in a radius of ~ 0.23 pc (*19*). This MDC hosts strong, highly variable Class II methanol (*20–25*) and water maser emission (*26–29*). In particular, an intense flare of the 6.7 GHz methanol maser was detected recently, increasing by more than a factor of 10 over a four month period, indicating active high-mass star formation associated with possible intense accretion bursts (*25*). We observed the source using the Atacama Large Millimeter/submillimeter Array (ALMA) at 3 mm (Band 3, Fig. 1A) and 1.3 mm (Band 6, Fig. 1B and 2) wavelengths. At resolutions of $0.03''–2''$, corresponding to 37–2400 au at the source distance, we discover a remarkable “spirals-bar-disk-outflow” complex in this MDC. Thermal molecular line emission in conjunction with the Class II methanol masers reveals a pseudodisk (or a rotating and infalling envelope, Fig. 3) and a Keplerian disk surrounding the embedded HMYSO (Fig. 4), which drives a bipolar outflow. The pseudodisk and the disk are fed by gas

streamers that are embedded in a $\sim 7,500$ au long bar-like structure (“bar”). The “bar” is connected to three prominent $\sim 20,000$ au long spiral arms as revealed by the 3 mm continuum emission. This discovery provides unprecedented insights into the complex interplay between the accretion disk and the hierarchical structures beyond it (Fig. 5).

Results

A Spiral-like system at core scale

ALMA 3 mm observations of continuum emission (Fig. 1A and Fig. 6) and molecular lines of H^{13}CO^+ and CCH (Fig. 7) reveal a distinct spiral system in I18134 that appears to channel material from beyond 20,000 au down to the central gravitational potential well. While spiral-arm-like structures induced by gravitational instability or by external perturbation such as flyby encounters are often witnessed in protostellar disks (13, 30–33), well-organized spiral arms in MDCs are rarely seen, with only a few candidates reported (15, 34–38).

Three prominent dusty spiral arms are visible in 3 mm continuum emission and can be modeled as logarithmic spirals (Materials & Methods; see Fig. 6), which are further confirmed in molecular line emission (see Fig. 7). One (S4) and two (S7-8) additional spiral arms can be identified in H^{13}CO^+ and CCH, respectively, trailing in the same direction as the dusty arms (see Fig. 7). Besides, four more spiral-like structures (S5, S6, S9, S10) are recognizable visually in H^{13}CO^+ and CCH, deviating from the trailing pattern of the dusty spirals (see Fig. 7). Different molecules might trace different parts of the cloud. To visualize the overall gas distribution, we stack the continuum emission and the peak intensity maps of H^{13}CO^+ and CCH with uniform weighting, after normalizing each to their maximum (fig. S1). The resulting composite map reveals an intricate spiral-like system.

The apparent spatial association alone is insufficient to conclusively validate these as bona fide structures; coherent kinematics are also needed. The intensity-weighted velocity maps of H^{13}CO^+ and CCH (see right panels in Fig. 7) and the position-velocity (PV) diagrams (see Fig. 8 and fig. S2) along the spiral arms present smooth velocity gradients or flat velocity profiles along the identified narrow structures, confirming their velocity-coherent nature. We further model the spiral arms in H^{13}CO^+ as the streamlines of a particle with an initial rotation, subject to the gravity of a central massive object (12, 39, 40) (Fig. 9). While this idealized kinematic model with a central mass of $50\text{--}80 M_{\odot}$ successfully reproduces the gas kinematics along S2 and S5, it can not capture the entire system’s dynamics, particularly the V-shaped velocity profiles of S1 and S2 that are likely indicative of the gravity-driven accretion of the cores lying within the filaments. Nevertheless, the velocity coherence along the spiral arms, coupled with the partial agreement between the model and the kinematics supports the idea that the gas flows in along the spiral arms with a mass inflow rate of $\sim 3.4 \times 10^{-4} M_{\odot} \text{ yr}^{-1}$ (Materials & Methods). This mass inflow rate is comparable with other high-mass star-forming regions with similar scale reported in the literature (35, 41–43)

A bar-like structure

A prolate structure (the central ellipse in Fig. 1A) with a aspect ratio ~ 1.5 ($\sim 5300 \times 3500$ au) has formed in the center of I18134, fed by the 20,000-au-scale spiral-like system. The prolateness of the structure is more distinctly visible in the composite map (fig. S1). It is further resolved in 1.3 mm continuum emission (Fig. 1B) and molecular line emission (e.g., DCN, Fig. 2B) at a high resolution of $0.3''$, showing a more prominent bar-like elongated structure (hereafter denoted as the “bar”). The “bar” is resolved into a bright compact object (called the “nucleus”) with slender extensions, referred to as streamers, stretching toward the southeast

and northwest. The slender streamers and the nucleus resemble a bar-like envelope linking the spiral system to the central protostar.

The spatial distribution of DCN strongly correlates with the 1.3 mm continuum emission (Fig. 2), tracing a similar bar-like structure. The centroid velocity map of DCN (Fig. 2B) shows that the northern spiral arm is blueshifted relative to the systematic velocity of I18134, suggesting a gas streamer infalling from the north to the “bar”. Additionally, the gas kinematics along the “bar” exhibit red-blueshifted symmetry around the “nucleus”, further supporting the idea that these streamers are transporting gas and converging toward the “nucleus”. This hypothesis is strengthened by the PV diagrams of various molecules cutting along the “bar” (fig. S3). Among these, DCN, H_2CO , HC_3N , and C^{18}O trace an elongated velocity-coherent structure spanning $\sim 6''$ (fig. S3 and S4), indicating that the “bar” may extend to a distance of $\sim 7,500$ au. The mass inflow rate from streamers to the “nucleus” is estimated to be $\sim 2.6 \times 10^{-4} \text{ M}_{\odot} \text{ yr}^{-1}$ (Materials & Methods), which is similar to the mass inflow rate along the spiral arms. Therefore, the “bar” plays a key intermediary role in channeling gas from the core-scale spiral-like system and fueling the very central “nucleus”.

Streamers penetrate the “bar” and connect to the nucleus

Zooming further into the “bar”, both DCN and CH_3OH show asymmetric spatial distribution (fig. S5). The distribution of DCN consists of three components: the diffuse ambient gas that forms the main body of the “bar”, a compact point source associated with the “nucleus”, and a small tail connecting to the “nucleus”. Notably, this tail extends along the southeast streamer. At the same position, a less apparent tail is also visible in the CH_3OH emission. Additionally, a second tail appears west of the “nucleus”, extending along the northwest streamer. The alignment of the tails and dusty streamers may suggest that the tails represent the terminal ends of the streamers where the gas is transported deep into the “nucleus”.

All the PV diagrams along the “bar” (fig. S3), except for that of C^{18}O , exhibit a diamond-shaped feature peaked at the “nucleus”. These diamond-shaped PV diagrams are characteristic of an infalling-rotating envelope (IRE), e.g. a non-rotationally supported envelope/pseudodisk (44–48). The continuity from the streamers to the pseudodisk suggests that the streamers are transporting material to a pseudodisk and the gas starts to rotate alongside the pseudodisk. We model the pseudodisk traced by CH_3OH thermal emission as an IRE to infer the geometry of the pseudodisk and the mass of the central mass (Fig. 3 and fig. S6). Despite the large uncertainty of the central mass, the model indicates a nearly face-on pseudodisk with an inclination $< 15^\circ$. Similar geometry and kinematics of the pseudodisk are also well revealed by other dense gas tracers such as CH_3CN lines (fig. S7).

The misaligned disk

Zooming into the “nucleus” with ALMA long-baseline observation at 1.3 mm (angular resolution of $\theta \approx 0.03''$, equivalent to 37 au), one single compact source which could be the disk is detected inside in the center of the “nucleus” (Fig. 4A). Besides the central compact component, one clear “mini-arm” can be identified in the south, while another three are tentatively detected in the north, west, and east, similar to the four-arm disk reported in (32). On the basis of 2-dimensional Gaussian fitting to the disk, the size and inclination of the disk are ~ 110 au and $\sim 75^\circ$, respectively. This inclination differs from the pseudodisk by more than 60° . Additionally, the presence of ^{12}CO bipolar outflow suggests the disk is not face-on. The combined evidence indicates that the disk and the pseudodisk are notably misaligned.

Jansky Very Large Array observations with a resolution of $\sim 0.2''$ led to the detection of 12 GHz Class II methanol masers oriented along the southeast-to-northwest direction (25), perpendicular to the CO bipolar outflow, indicating that the Class II methanol masers may

trace the disk (Fig. 4b). Specifically, the blueshifted maser cluster corresponds to the southern spiral arm seen in the long-baseline observation, the redshifted cluster aligns with the northern arm, and another cluster (in gray color) seems to align with the outflow (Fig. 4b). The linear distribution of the Class II methanol masers suggests that the disk is likely viewed at a larger inclination than the pseudodisk. This further supports that the disk is misaligned with the pseudodisk. Meanwhile, the orientation of the linear distribution likely corresponds to the major axis of the disk traced by the maser which also deviates from the major axis of the continuum disk. This might suggest that the masers and the long-baseline continuum trace different disk structures. For example, the maser and the continuum trace the outer and inner disk, respectively, and they might also be misaligned.

The most remarkable feature is that the velocity distribution of the masers is opposite to the velocity field of the pseudodisk (see Fig. 4C and the cartoon in Fig. 5C). The velocity reversal may suggest opposite signs for the inclination of the disk traced by the maser and the pseudodisk. Previous observations have detected misalignment of the orientation between the disk and the envelope in low-mass star forming cores (49–51). In extreme cases, the Keplerian disk could be counter-rotating relative to the pseudodisk. While mechanisms for this extreme scenario have been proposed in low-mass star-forming regions: the interaction with the spiral arm in a circum-multiple disk (52) and non-ideal magneto-hydrodynamics effects (53, 54), it is still theoretically unclear whether this scenario could happen in massive disks. Anyway, here we provide a firm detection of a misaligned disk surrounding a HMYSO.

The opposite signs for the inclination could also arise from the nearly face-on orientation of the pseudodisk and the potential wobbling due to the non-uniform angular momentum transfer to the Keplerian disk via asymmetric accretion flows, leading to a few tens of degrees of shift in the spin axis orientation (55, 56). To better visualize this effect, fig. S8 provides a schematic representation of this inclination difference. After excluding the maser cluster aligned with the outflow direction, the remaining 12 GHz Class II methanol masers follow Keplerian rotation very well (Materials & Methods and Fig. 4c). We perform Keplerian curve modeling on the spatial-kinematics of the masers in the projected position-velocity diagram. The best-fit scaled enclosed mass ($M_{*,d} \times \sin^2 i$ where $M_{*,d}$ is the dynamic mass and i is the inclination of the disk) is $1.93 M_{\odot}$. If we take the best-fit inclination of the pseudodisk as the inclination of the disk, the mass of HMYSO $M_{*,d}$ would be over $180 M_{\odot}$ which is almost the total mass of the MDC. Thus, the inclination of the maser disk should be larger than that of the pseudodisk, which further suggests the misalignment between the pseudodisk and the maser disk. Radio continuum emission from the central UC HII region suggests that the spectral type of the central star is between B3 and B0 (18), corresponding to a stellar mass of 8-16 M_{\odot} (57). Assuming this stellar mass range, the inclination of the maser disk would be 20° to 30° .

As mentioned above, the “nucleus” in MDC IRAS 18134-1942 is fed by gas streamers within the elongated bar-like structure, indicating that the formation of the misaligned disk may be induced by gas infall, as suggested in numerical simulations (58). Multiple or episodic gas acquisition events through the large-scale barred spiral-like system during the gas accretion and angular momentum build-up of the disk may naturally lead to the kinematical misalignment (or even counter-rotation) of components in the “nucleus”.

In addition, the shock tracers, H_2 , SiO thermal emission, and 22 GHz water masers, are well-aligned, but they deviate by approximately 30° from the direction of the ^{12}CO outflow (left panel in Fig. 2C and fig. S9). The wobbling disk due to the asymmetric accretion flow could also be the reason for the misalignment between the ^{12}CO outflow and the shock, and the potential jet precession revealed by ^{12}CO high-velocity emission (fig. S10).

The disk-mediated accretion rate of the HMYSO, inferred from CO outflow emission, is

$\sim 2.8 \times 10^{-6} M_{\odot} \text{ yr}^{-1}$ (Materials & Methods), which is two orders of magnitude smaller than the mass inflow rate along the spiral arms and the streamers. Since we assume ^{12}CO emission is optically thin, and due to the potential missing flux caused by the lack of short spacing of the interferometer, this accretion rate would be the lower limit of the exact accretion rate. However, the estimated accretion rate is consistent with the accretion rates of high-mass star formation regions reported in (59). In particular, a strong correlation between the accretion rate \dot{M}_{acc} and luminosity-to-mass ratio $L_{\text{bol}}/M_{\text{clump}}$ is reported: $\log(\dot{M}_{\text{acc}}) = 0.8 \log(L_{\text{bol}}/M_{\text{clump}}) - 5.8$. With a $\log(L_{\text{bol}}/M_{\text{clump}})$ of 0.65 (19), $\log(\dot{M}_{\text{acc}})$ of I18134 from this relation would be -5.28 which is closed to the estimated $\log(\dot{M}_{\text{acc}})$ of -5.55. The drastic decrease from the mass inflow rate of the streamers to the disk-mediated accretion rate suggests that the rotating envelope and protostellar disk may play a crucial regulatory role in the mass growth of the protostar.

Discussion

The discovery of the “spirals-bar-disk-outflow” complex (see the cartoon in Figure 5) in MDC IRAS 18134-1942 provides the clearest observational evidence that HMYSOs can efficiently assemble their masses through multi-scale gas accretion within a dense core (~ 0.1 pc). Gas flows in from spiral arms down to the “bar”, and then finally onto the disk. The gas transfer rate remains relatively constant ($\sim 10^{-4} M_{\odot} \text{ yr}^{-1}$) from the spiral system to the “bar”, suggesting a hierarchical but continuous mass infall process. The asymmetric gas inflows, ending at the disk, could trigger the accretion bursts of the HMYSOs (60, 61), which in turn could explain the methanol maser flares. Such inflows could also inject angular momentum non-uniformly to the HMYSO, resulting in the disk wobbling and the jet precession. The disk wobbling could cause the misalignment of the disk and envelope. Our discovery manifests that barred spiral-like structures within MDCs play an important role during the gas accretion and angular momentum build-up of massive disks. Future studies of more similar systems will be crucial for unraveling the mystery of high-mass star formation as well as massive disk formation. Furthermore, from the visual impression alone, the “spirals-bar-disk-outflow” complex (Figure 5) closely resembles the morphology of a barred spiral galaxy with an active galactic nucleus (AGN) despite their very different physical scales and central engines (HMYSO versus supermassive black hole). This work demonstrates that spiral systems and bar-like structures can be formed not only in self-gravitating rotating systems like galactic discs (for example, see some state-of-the-art simulation of the formation of galactic discs in very gas-rich environments (62–64)) but also in high-mass star formation regions. This suggests that in certain systems these structures are closely linked to the mass transport process. Detailed comparison to barred spiral galaxies is beyond the scope of this work. However, insight from the formation and evolution of galaxies and AGNs would provide valuable inspiration for the high-mass star formation community, and vice versa.

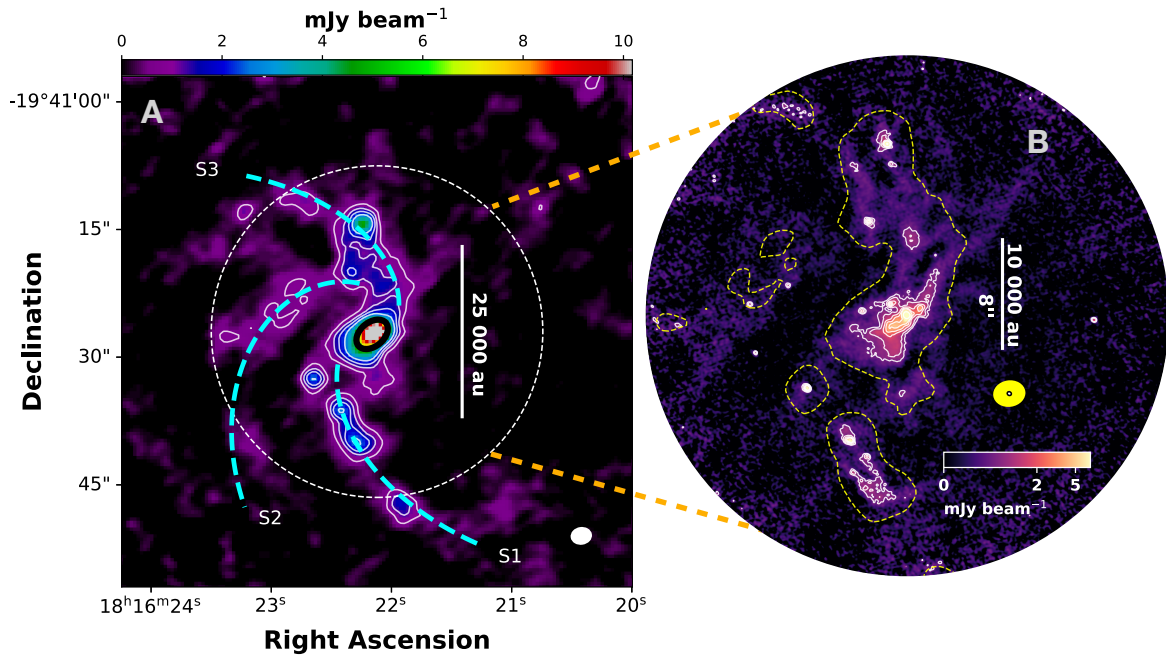


Figure 1 | Continuum images of ALMA 3 mm and 1.3 mm observations. A, ALMA 3 mm continuum image of IRAS 18134-1942, showing a bright central core, elongated filamentary structures extending from the center, and several cores forming along those. The white contours are $[3, 5, 7, 10, 15, 30, 50, 90] \times \sigma_{3\text{mm}}$, where the rms noise $\sigma_{3\text{mm}}$ is 0.25 mJy per beam. The $2.15'' \times 1.71''$ restored beam is plotted at the lower right corner. The cyan dashed logarithmic spiral curves are plotted for visual guidance. The white dashed circle represents the field of view of the 1.3 mm observation. The black ellipse ($4.2'' \times 2.8''$ from two-dimensional Gaussian fitting) at the center represents the bar structure unresolved in 3 mm continuum. B, ALMA 1.3 mm continuum image. The yellow dashed contour marks the $3 \times \sigma_{3\text{mm}}$ of the 3 mm continuum emission. The white contours are $[3, 5, 9, 13, 17, 50] \times \sigma_{1.3\text{mm}}$, where $\sigma_{1.3\text{mm}} = 0.25$ mJy per beam. The $0.31'' \times 0.27''$ restored beam of the 1.3 mm continuum image is shown as a black ellipse with black edge over the 3 mm beam shown as a yellow ellipse between the scalebar and the colorbar.

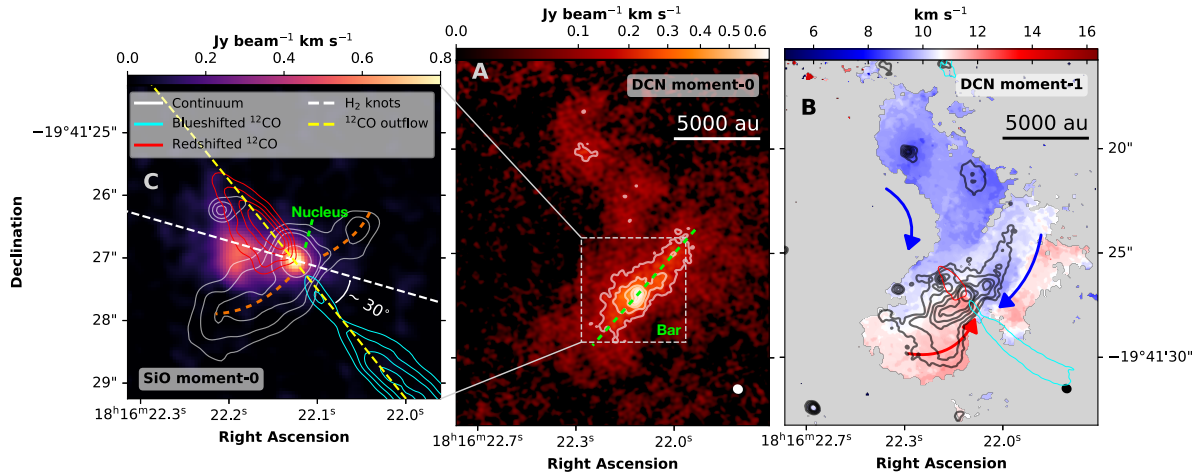


Figure 2 | DCN integrated intensity and velocity maps showing infalling and converging streamers feeding the central nucleus, and SiO emission tracing the shocked gas and ^{12}CO emission tracing the outflow gas. A Integrated intensity of DCN. The contours are at $[3, 5, 7, 9, 11] \times \sigma_{\text{DCN}}$ where $\sigma_{\text{DCN}} = 0.05 \text{ Jy beam}^{-1} \text{ km s}^{-1}$. B, Centroid velocity map of DCN. The black contours are the 1.3 mm continuum emission (same as that in Fig. 1B). The blue and red arrows mark the proposed gas kinematics: three gas streamers converge to the central nucleus. It is worthy noting that the northern streamer is part of the large-scale spiral arm, and the other two are consistent with the dust streamers revealed by 1.3 mm continuum emission. The synthesized beam is shown at the lower right corners of A and B. C, Redshifted (red contours) and blueshifted (cyan contours) ^{12}CO emission is overlaid of the SiO integrated intensity (colorscale). The red- and blueshifted outflow gas integrated between $[20, 50] \text{ km s}^{-1}$ and $[-30, 0] \text{ km s}^{-1}$, respectively. The white contours showing the 1.3 mm continuum emission are $[9, 13, 17, 50] \times \sigma_{1.3\text{mm}}$ to emphasize the streamers. The white dashed line represents the direction of H_2 knots (25, 65) while the yellow dashed line shows the direction of ^{12}CO outflow. The orange dashed lines represent the streamers in 1.3 mm continuum. The outermost contours of the red and blue lobes are also shown in B.

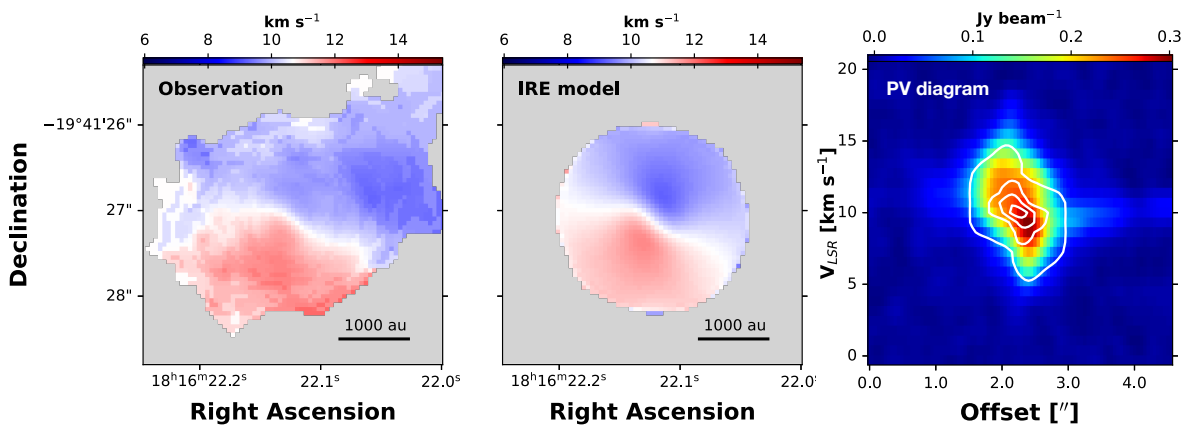


Figure 3 | The comparison between the kinematics of the CH_3OH observation and the best-fit model. The left and middle panels show the centroid velocity maps of the observation and the model, respectively. The PV diagrams of the observation (colormap) and the model (white contours) are shown in the right panel. Contour levels are 20%, 40%, 60%, and 80% of the peak intensity of the model.

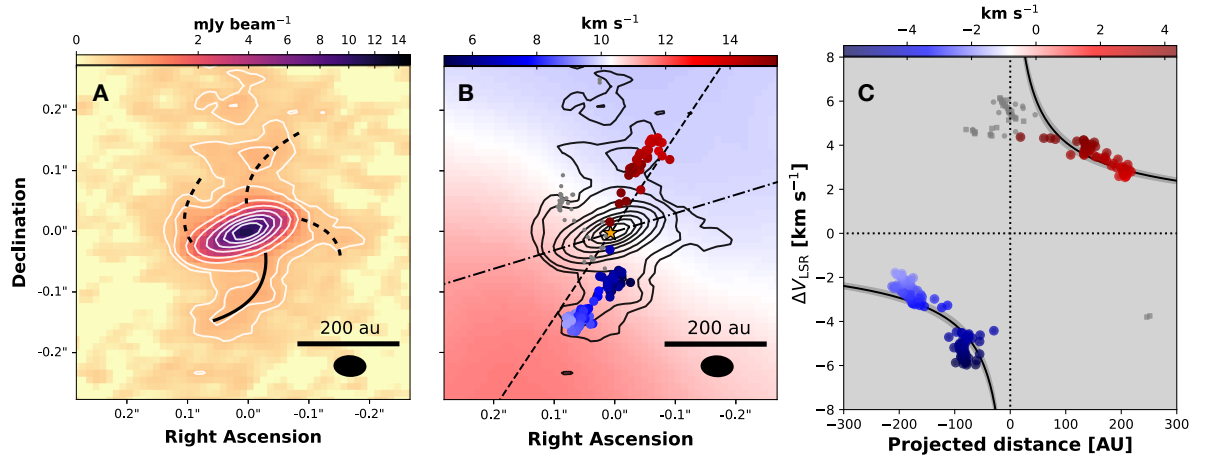


Figure 4 | ALMA long-baseline (1.3 mm), QUARKS (1.3 mm), and VLA 12 GHz methanol maser observations. A, ALMA archival long-baseline 1.3 mm continuum observation ($\theta \approx 30$ mas). The contour levels are at $[3, 5, 15, 30, 60, 90, 120, 150] \times \sigma_{\text{lb}}$ where σ_{lb} is 0.06 mJy per beam. The black curve sketches the southern mini-arm and the three dashed curves mark the tentative mini-arms in the disk. B, The intensity-weighted velocity map of CH₃OH 4₂ - 3₁ E1 vt = 0 (background) and 12 GHz methanol maser spots. The line-of-sight velocity of the selected maser spots is color-coded. The black dashed line indicates the direction of the PV cut for the maser spots which is also the direction of the largest velocity gradient of CH₃OH thermal line emission. The black dash-dotted line is the position angle of the inner disk from the 2-dimensional Gaussian fitting. The orange star marker represents the peak of the long-baseline continuum. The black contours are the same as in panel A. C, The PV diagram of 12 GHz methanol maser projected to the PV cut in panel B. The black curves represent the Keplerian rotation curve with a scaled enclosed mass $M_{*,d} \times \sin^2 i$ of $1.93 M_{\odot}$. The grey spots in panels B and C are the excluded maser spots.

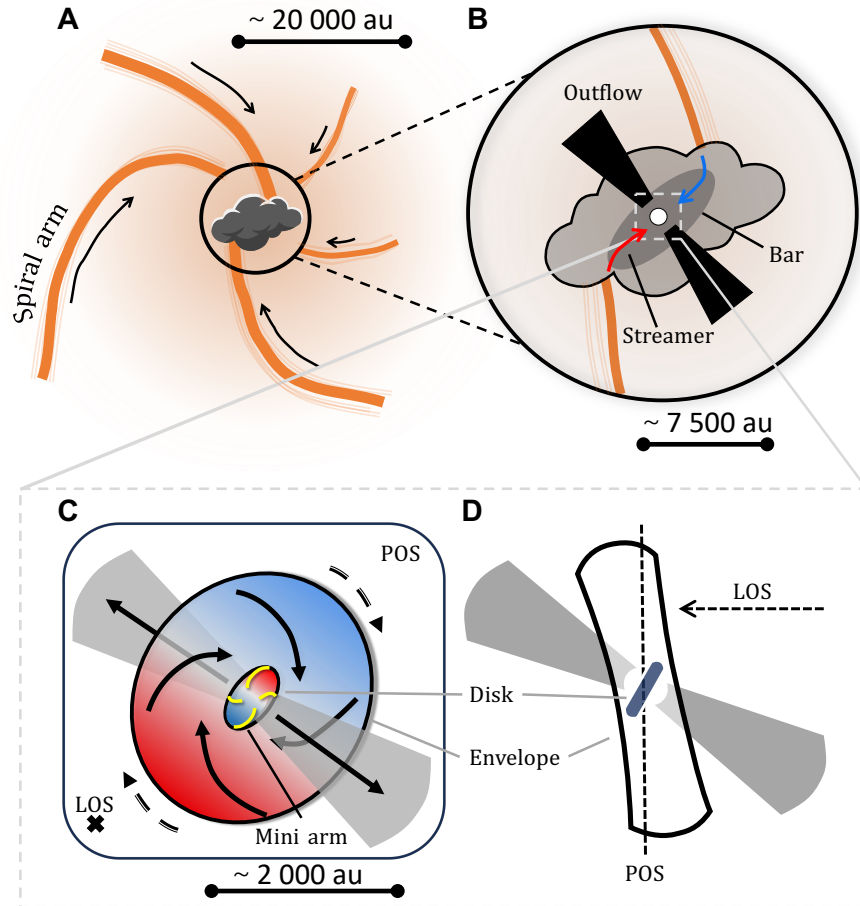


Figure 5 | A schematic view of the complex system in IRAS 18134-1942. Panel A: Spiral arms with sizes of $\times 10,000$ au. Panel B: The “bar” (~ 7500 au) and streamers (blue and red arrows) revealed by 1.3 mm continuum emission. Black cones show molecular outflow traced by ^{12}CO . Panel C and D show the front view and side view of the envelope as well as the embedded disk, respectively. ‘POS’ denotes ‘Plane of Sky’ while ‘LOS’ means ‘Line of Sight’. The most remarkable feature is that the velocity distribution of the disk (inner ellipse; $\sim 100\text{--}400$ au) traced by 12 GHz Class II methanol masers is opposite to the velocity field of the envelope/pseudodisk (outer ellipse; $\sim 1000\text{--}2000$ au). The yellow curves in panel C show the mini-arms of the disk.

Materials & Methods

ALMA observations and data reduction

ALMA 3 mm observations

IRAS 18134-1942 was observed under the project “ALMA Three-millimeter Observations of Massive Star-forming regions (ATOMS)” with Atacama Compact 7 m Array (ACA) and 12 m ALMA arrays (C43-3 configuration) using the Band 3 receiver (66) on 2019 November 1-3 (Project ID: 2019.1.00685.S; PI: Tie Liu). The standard calibration was done using Common Astronomy Software Applications (CASA) package (67) 5.6. The ACA data and 12 m-array data were combined and imaged using the same version of CASA with natural weighting, yielding an angular resolution of $2.15 \text{ arcsec} \times 1.72 \text{ arcsec}$ (position angle of -81.4°) for the 3 mm continuum emission. The continuum image is shown in Fig. 1; The pixel size is $0.4''$ and it achieved an rms noise of $\sim 0.25 \text{ mJy beam}^{-1}$. We refer to the survey description paper (68) for the observations and data reduction details.

ALMA 1.3 mm observations

We conducted ALMA Band 6 (69) observations of IRAS 18134-1942 ACA and 12 m arrays (C-2 and C-5 configurations) under the project “Querying Underlying mechanisms of massive star formation with ALMA-Resolved gas Kinematics and Structures (QUARKS)” (project code: 2021.1.00095S, PIs: Lei Zhu, Tie Liu, and Guido Garay) on 2023 April 17 (ACA), 2024 March 19 (C-2) and 2022 August 15 (C-5). The calibration, image, and self-calibration were done using CASA 6.5. We cleaned the continuum image and the cube data with a pixel size of $0.05''$ using the *briggs* weighting. The *robust* parameter is adopted as 0.5. We conducted three rounds of phase-only self-calibration with a shortest solution interval of 12 s. For the details of observations and data reduction, we also refer to the survey description paper (70). We achieved an angular resolution of $0.30 \text{ arcsec} \times 0.27 \text{ arcsec}$ (position angle of 66.8°) and an rms noise on the continuum emission of $\sim 0.25 \text{ mJy beam}^{-1}$. For the highest-resolution observation, we use the self-calibrated product image from the ALMA science archive (project code: 2021.1.00455.T, PI: Todd Hunter). The synthesized beam size is $0.05 \text{ arcsec} \times 0.03 \text{ arcsec}$ (position angle of 87.4°). The rms noise is $\sim 0.06 \text{ mJy beam}^{-1}$.

Spiral-arm-like structures

Morphology

We first characterize spiral-like filaments (hereafter spiral arms) on the 3 mm continuum map. For simplicity, we model the spiral arms as logarithmic spirals, described by $R(\theta) = R_0 e^{a\theta}$, where R_0 is the starting radius of the spiral, a is the growth rate of the spiral, and the pitch angle is given by $\arctan |a|$. The starting radius R_0 of each spiral arm is manually determined from the projected polar plot. The polar plots were made via Python package *polarTransform*. Using the logarithmic spiral curve, we generated spiral model images via the Bresenham Line Algorithm and convolved them with a 2-dimensional Gaussian kernel with the same full width at half maximum (FWHM) as the synthesized beam (fig. S11A). By calculating the Pearson correlation coefficient between the model images and the 3 mm continuum map, we identified the spiral model that best matches the original continuum map (fig. S11B). The best fit of a is robust against the choice of the FWHM. The best match spiral arms S1, S2, and S3 are outlined as cyan dashed curves in Fig. 1. The pitch angles of S1-3 are 49° , 34° , and 52° , respectively. The pitch angles of S1 and S3 are quite similar which might suggest that the two arms form a

symmetric grand-design spiral system.

The molecular gas distribution also exhibits a similar spiral pattern. Fig. 7 presents the peak intensity and centroid velocity maps of $\text{H}^{13}\text{CO}^+ J = 1 - 0$ and $\text{CCH } N_{J,K} = 1_{3/2,2} - 0_{1/2,1}$. The spiral pattern of the gas distribution is more distinctly visible in molecular gas. We employ a similar approach to identify and characterize the spiral arms in the peak intensity maps. The emission from S2 is more extended in H^{13}CO^+ than in the continuum emission. The parameter a of S2 measured in the continuum map is replaced by the best match a when matching the model with the emission from H^{13}CO^+ , assuming that both map the same gas. One (S4) and three (S4, S7, S8) additional spiral arms are identified in H^{13}CO^+ and CCH, respectively, as indicated by the orange and red dashed curves. While a logarithmic spiral curve was used to depict the gas distribution for simplicity, it can not fully capture the entire morphology. We outline manually additional filamentary structures in these peak intensity maps, as orange and red dotted lines. To examine the overall gas distribution, we stack the normalized peak intensity maps of H^{13}CO^+ and CCH alongside with the 3 mm continuum map with uniform weighting in fig. S1 (this neglects the relative abundance between dust, H^{13}CO^+ , and CCH).

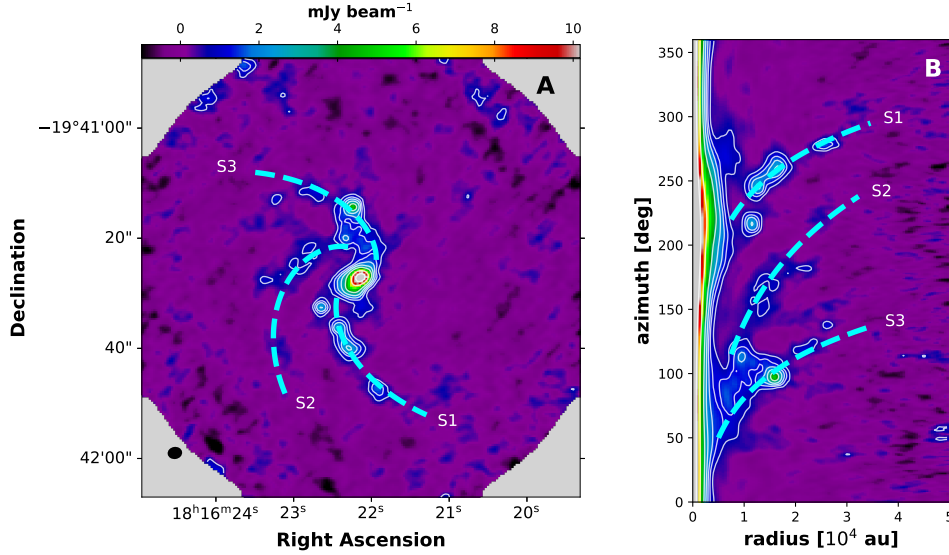


Fig. 6 | 3 mm continuum emission and the identified spiral arms. Panel A shows 3 mm continuum emission. Panel B shows the same emission as panel A but is projected with respect to the clump center and replotted as a function of radius and polar angle. The white contours at both panels are at the same levels as in Fig. 1.

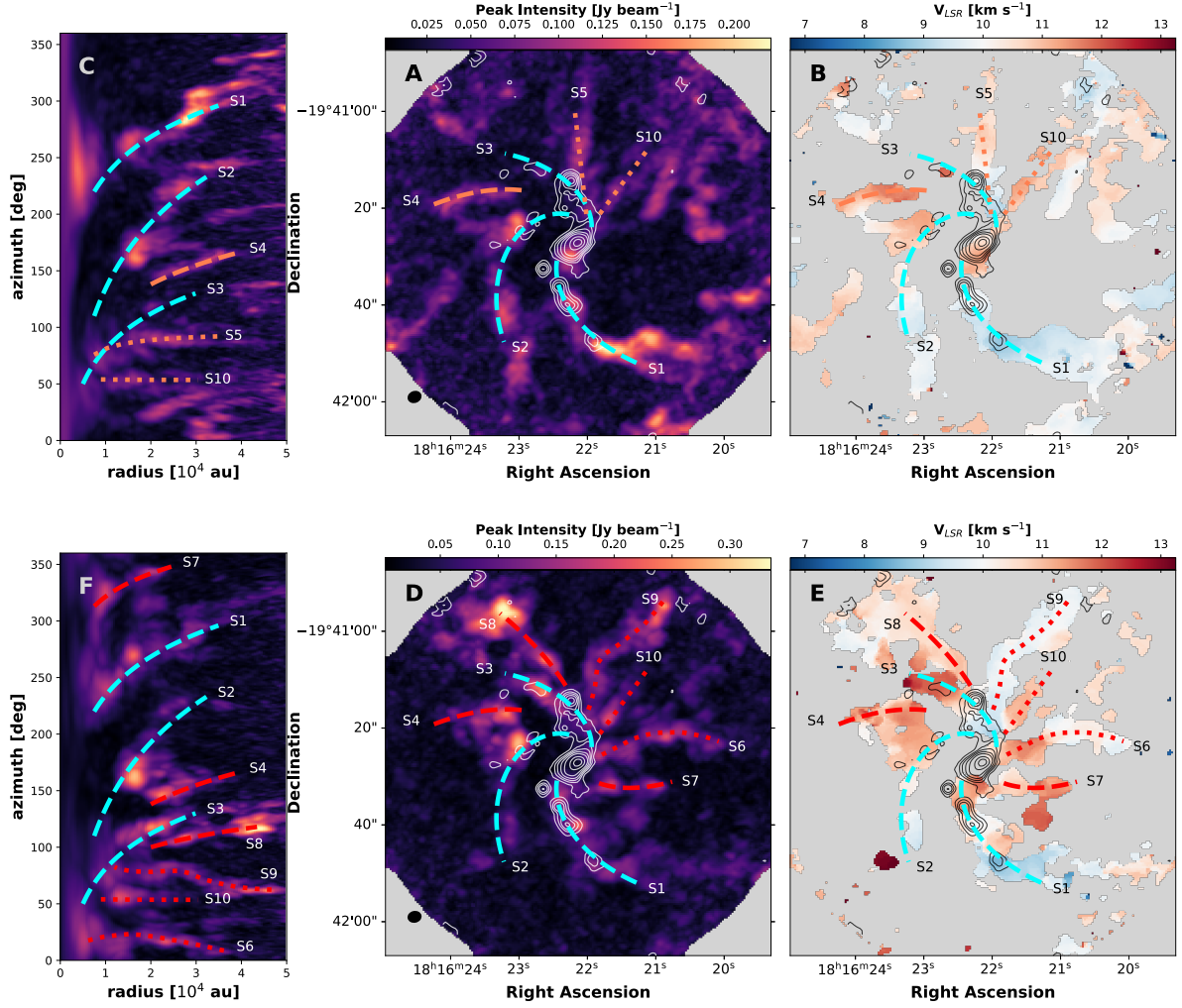


Fig. 7 | The spiral-like system traced by H^{13}CO^+ and CCH. A, The peak intensity map (8th moment map) of H^{13}CO^+ . The cyan dashed curves trace the spiral arms identified in the 3 mm continuum emission. The spiral arms identified in H^{13}CO^+ are plotted as orange dashed curves and the filaments outlined manually are plotted as coral dotted curves. B, The centroid velocity map, depicting the kinematics of the gas. C The polar projection of the peak intensity map A. D-F Same as A-C, but for CCH. The spiral arms identified in H^{13}CO^+ are plotted as red dashed curves and the filaments outlined manually are plotted as red dotted curves. All the contours are 3 mm continuum emission at the same levels as Fig. 1.

Gas Kinematics

The PV cuts are placed along the curves we identified in the previous section. The PV diagrams are shown in Fig. 8 and fig. 2, which reveal that the identified structures are velocity-coherent filaments. The velocity gradients seen in the PV diagrams may indicate that the gas is infalling to the center of the clump driven by the gravitational force of the central object.

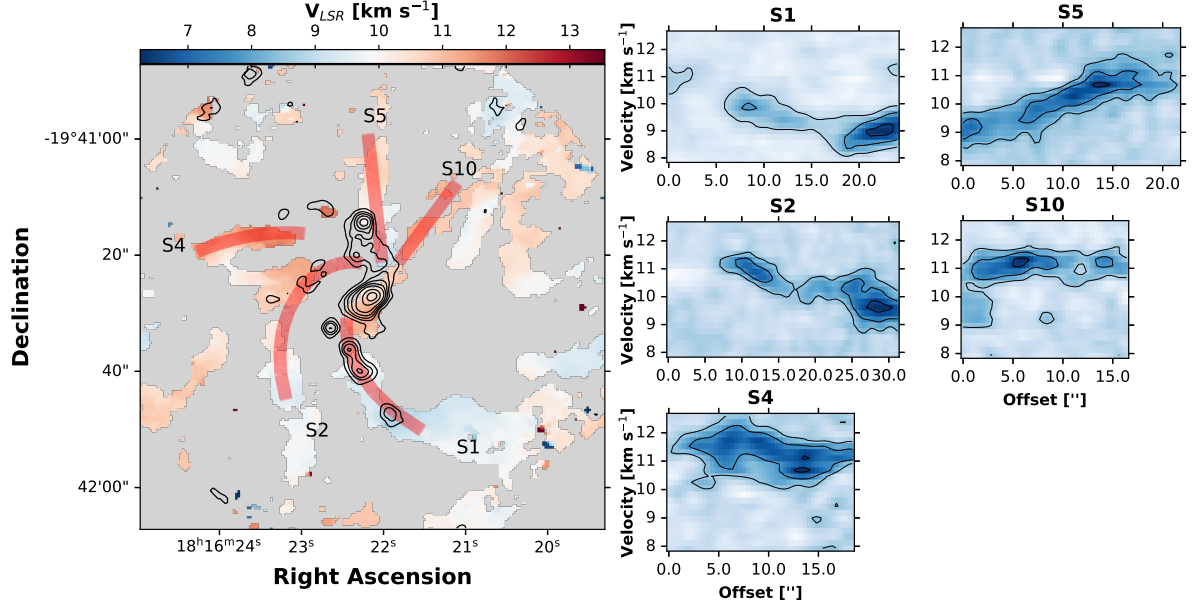


Fig. 8 | The velocity coherent filaments traced by H^{13}CO^+ . Left shows centroid velocity map of H^{13}CO^+ , with 3 mm continuum emission overplotted. The filaments identified previously are shown as red bands. Right shows position-velocity diagrams along each streamers in H^{13}CO^+ . The offset is from the center outward. The contours are drawn at the level of 20%, 50%, and 90% of the peak intensity of the PV diagrams.

Infalling-rotating particle trajectory

We model the kinematics of the filaments observed with H^{13}CO^+ to validate whether the velocity gradient is consistent with infall motion using an analytic solutions (39, 40) of a particle moving within a rotating cloud toward a central mass. The model provides both the plane-of-sky position and the line-of-sight velocity along an infalling streamline. The model is defined by a central point mass, the inclination angle of the angular momentum vector of the rotating plane, and the angular velocity of the cloud assuming a rigid body rotation. The major inputs are the initial position and velocity of the particle in spherical coordinates.

We manually adjust the model and streamline parameters to find the best match parameter set. Based on the observed gas morphology, we assume the inclination angle to be between 0° to 20° (where 0° represents a face-on view). The model that best reproduces the observed features is obtained using the initial distance of 52,000 au, the position angle of 21° , and the polar angle of 70° for S2, and the initial radius of 35,500 au, the azimuthal angle of 176° , and the polar angle of 40° for S5. The position angle is measured from the north in a clockwise direction, and the polar angle is measured from the spin axis of the plane whose inclination angle is 10° . The angular velocity is assumed as $4 \times 10^{-14} \text{ rad s}^{-1}$ and the initial radial velocity is 0.6 km s^{-1} . Fig. 9 shows the streamline trajectories (in coral) assuming a central mass of $50\text{--}80 M_\odot$ in S2 and S5 which spatially align with the emission in the peak intensity map (left column). The middle column shows the centroid velocity and also the trajectories color-coded by line-of-sight velocity. The right column presents the kernel density estimate (KDE) of the centroid velocity versus the projected distance from the central mass measured in the middle column.

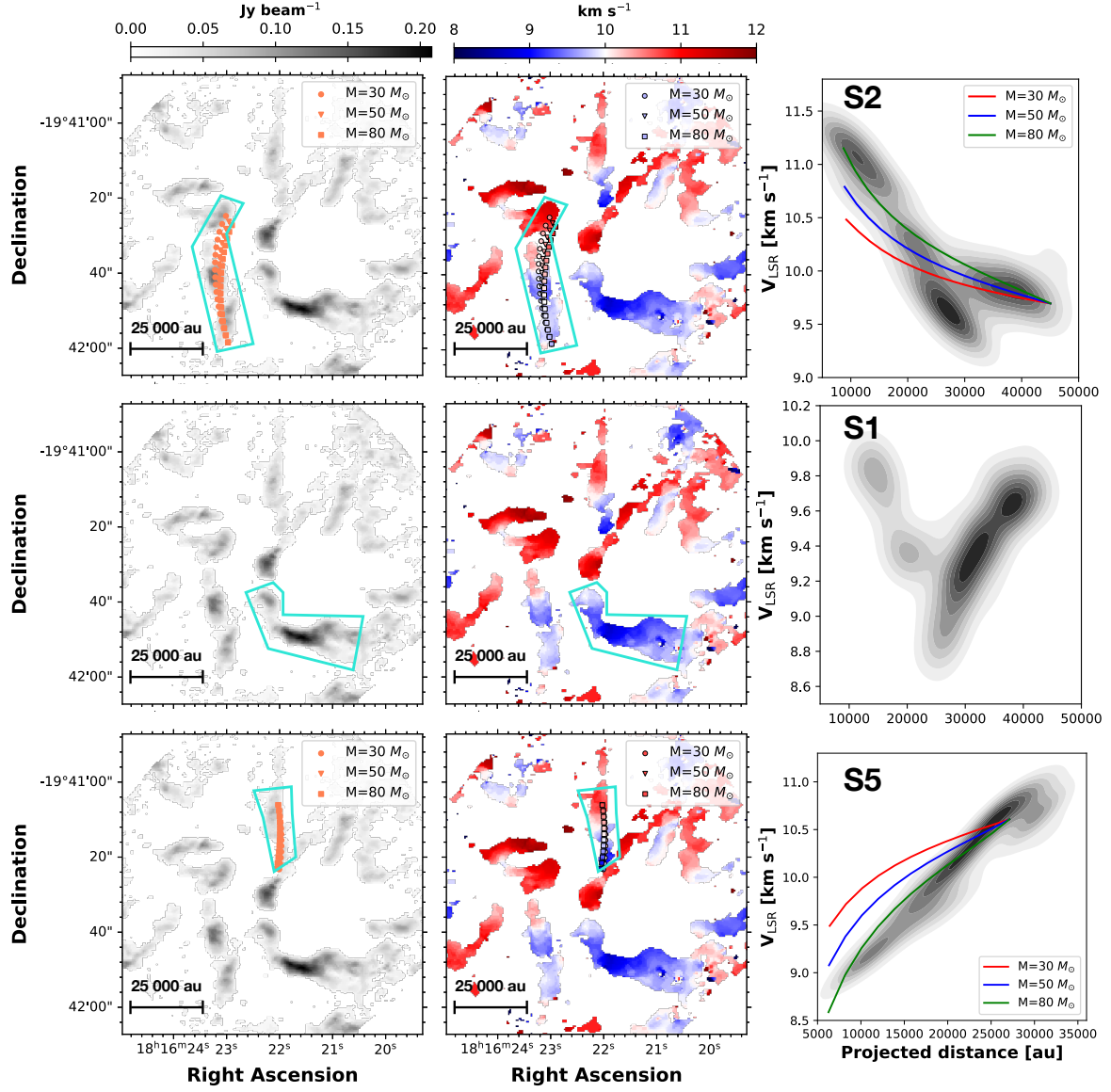


Fig. 9 | The kinematics observed in H^{13}CO^+ and the model trajectories of the infall-rotating particle. Rows correspond to S2 (first row), S1 (second row), and S5 (third row), while columns show peak intensity maps (first), centroid velocity maps (second), and kernel density distribution of centroid velocity versus projected distance (third).

IRE modeling

Based on the spatial distribution and velocity map, the $\text{CH}_3\text{OH } 4_2 - 3_1 \text{ E1 vt} = 0$ emission is expected to trace the pseudodisk. Here we model the pseudodisk as a flattened infalling and rotating envelope (IRE) with the publicly available code FERIA (71). The central mass $M_{*,e}$, the centrifugal radius r_{CB} , the outer radius of the IRE r_{out} and the inclination i are treated as free parameters. The position angle of the IRE model is fixed to the velocity gradient observed in the centroid velocity map. Note that the uncertainties arising from the simplicity of the model could dominate over the observational noise. For this reason, instead of conducting a precise fitting method like MCMC, we employed a χ^2 grid search to explore the parameter space in this study. To reduce computational time, we began with a coarse χ^2 grid search to constrain the parameter ranges, followed by a fine grid search. The parameter ranges for the fine grid search are summarized in table S1. The best-fit parameter set with the lowest χ^2 value includes $M_{*,e}$ of $45 M_\odot$, i of 6° , r_{CB} of 60 au, and r_{out} of 950 au (fig. S6). As shown in Fig. 3, the best-fit model can reproduce the overall kinematics, especially the curvature shown on the centroid velocity maps—representing the local velocity $\sim 10.6 \text{ km s}^{-1}$ —due to the infalling and rotating kinematics. Notably, the χ^2 distribution in the $i - M_{*,e}$ space reveals a ridge-like pattern, where central mass and inclination are correlated. The model is insensitive to central mass but tightly constrains the inclination to $< 15^\circ$. The model only considers a central point mass, and the best-fit $45 M_\odot$ is too massive for a protostar at a very early stage. Consequently, despite the uncertainty in the central mass, the IRE modeling robustly indicates a nearly face-on pseudodisk.

Dynamics of the maser disk

We manually selected two blueshifted and redshifted maser clusters in the southeast and northwest for the reason that the northeast cluster (grey spots in Fig. 4A) is possibly associated with the outflow due to the similar velocity and direction compared with the 22 GHz water masers and the H_2 knots (25) (see fig. S9), or it is associated with the tentative eastern spiral arm. After projecting the maser spot onto a position-velocity cut, we modeled the spatial-kinematics of the maser using a Keplerian rotation model, treating the scaled enclosed mass ($M_{*,d} \times \sin^2 i$ where $M_{*,d}$ is the dynamic mass and i is the inclination of the disk), and the system velocity as free parameters. The position angle of the position-velocity cut was fixed as the direction of the steepest velocity gradient in the ALMA observation. The disk center was assumed to be the peak of the long-baseline 1.3 mm continuum. The best-fit Keplerian rotation profile is shown in the position-velocity diagram in Fig. 4. The scaled enclosed mass was estimated using the least-square fitting, implemented in SciPy, to be $M_{*,d} \times \sin^2 i = 1.93 \pm 0.07 M_\odot$.

Misalignment between outflow and shocked gas

We detect the outflow emission traced by ^{12}CO covered in our frequency range. fig. S9A shows the red- and blueshifted outflow gas integrated between $[20, 50] \text{ km s}^{-1}$ and $[-30, 0] \text{ km s}^{-1}$, respectively, where it is free of ^{13}CO and C^{18}O emissions. Along with the ^{12}CO outflow gas, the shock-induced SiO, H_2 , and 22 GHz water maser emission are also shown in the same figure. SiO, H_2 , and 22 GHz water masers share a similar extended direction $\sim 253^\circ$, implying a common shock origin, likely driven by the jet. The ^{12}CO outflow is in a different direction, differing from the jet direction by $\sim 30^\circ$.

Mass assembly rate at different scales We determine the column density of H^{13}CO^+ $J = 1 - 0$, CCH $N_{J,K} = 1_{3/2,2} - 0_{1/2,1}$ assuming optically thin conditions with (72):

$$N = \frac{3h}{8\pi^3 |\mu_{lu}|^2} \frac{Q_{\text{rot}}}{g_u} \exp\left(\frac{E_u}{kT_{\text{ex}}}\right) \left[\exp\left(\frac{h\nu}{kT_{\text{ex}}}\right) - 1 \right]^{-1} \frac{\int T_{\text{B}} d\nu}{T_{\text{ex}}}, \quad (1)$$

where h , $|\mu_{lu}|^2$, Q_{rot} , g_u , E_u , k , T_{ex} , ν , and T_{B} are the Planck constant, the dipole matrix element, the rotational partition function, the level degeneracy, the upper state energy, the Boltzmann constant, the excitation temperature which is adopted as 20 K, the frequency of the transitions, and the brightness temperature. The $|\mu_{lu}|^2$, Q_{rot} , g_u , and E_u are taken from CDMS Database (73). The mass of the inflow is then calculated through

$$M_{\text{inflow}} = X^{-1} m_{\text{H}_2} A D^2 \sum_{i,j} N_{ij}, \quad (2)$$

where X , m_{H_2} , A , D , N_{ij} are the molecular abundance relative to H_2 , the mass of a hydrogen molecule, the angular area of a pixel, the source distance, and the column density at the pixel ij . We calculate the mass of the inflows seen in H^{13}CO^+ emission and the rest seen in CCH emission. We assume the abundances of H^{13}CO^+ and CCH to be 1.28×10^{-10} (74) and 3.72×10^{-8} (75), respectively. The total masses of the H^{13}CO^+ and CCH spiral system are 22.9 and $3.4 M_{\odot}$, respectively. Assuming that the velocity gradient ∇V_{\parallel} , which is the velocity profile in the Moment 1 maps, is due to the inflow, we further calculate the inflow rate \dot{M}_{\parallel} via (76):

$$\dot{M}_{\parallel} = \frac{\nabla V_{\parallel} M_{\text{inflow}}}{\tan \theta}, \quad (3)$$

where θ is the inclination angle. We assume the inclination angle to all be 45° except for S2 and S5, which are 30° and 60° , respectively, based on the previous infall-rotating particle trajectory modeling. The total inflow rate for the spirals detected in H^{13}CO^+ and CCH is $3.4 \times 10^{-4} M_{\odot} \text{ yr}^{-1}$.

We estimate the total mass of the “bar” from the 1.3 mm dust continuum emission. In the optically thin limit, the mass can be calculated as

$$M = R_{\text{dg}} \frac{F_{\nu} D^2}{\kappa_{\nu} B_{\nu}(T)}, \quad (4)$$

where R_{dg} is the gas-to-dust ratio, F_{ν} is the flux density, κ_{ν} is the dust opacity per gram of dust, and $B_{\nu}(T)$ is the Planck function at the dust temperature of T . We use *astrodendro* algorithm to extract the flux of the “bar” from the dendrogram which is an abstraction of the changing topology of the isosurfaces of a two-dimensional image as a function of contour levels (77). The algorithm organizes hierarchical structures into “trees” consisting of “branches”, formed by combining “leaves” in the terminology of *astrodendro*. The following parameters are used in computing the dendrogram: the minimum pixel value *min-value* is $3\sigma_{1.3\text{mm}}$; the minimum difference in the peak intensity between neighboring structures *min-delta* = $1\sigma_{1.3\text{mm}}$; and the minimum number of pixels required for a structure to be considered an independent entity *min-npix* = N_{beam} , where N_{beam} is the number of pixels enclosed in the synthesized beam. Fig. 10 shows the identified “bar” as a tree and the potential protostars as leaves. We subtract the fluxes of two luminous leaves from the total flux of the tree to obtain the flux of the extended structure.

Adopting a R_{dg} of 100, κ_{ν} of $1 \text{ cm}^2 \text{ g}^{-1}$ (78) (interpolated to 1.3 mm with the dust opacity index β of 1.6), and a temperature of 20 K, the mass of the “bar” is $6.2 M_{\odot}$. Besides the rotation, there is also a global velocity gradient of $\sim 41 \text{ km s}^{-1} \text{ pc}^{-1}$ along the “bar” as

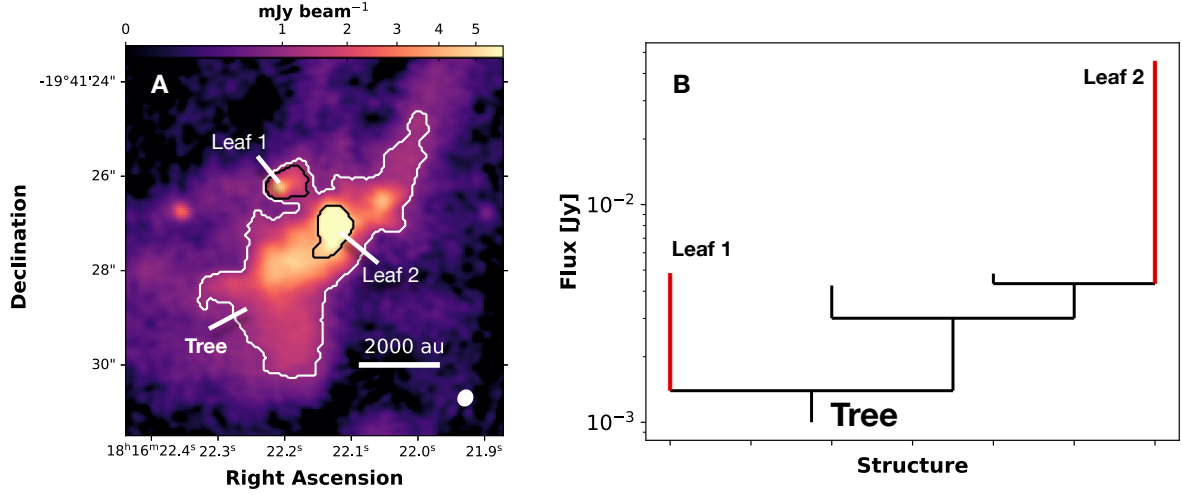


Fig. 10 | The hierarchical structure of the “bar”. A, The 1.3 mm continuum overlaid with the “tree” structure as white contour and “leaves” structure as black contours. The most luminous leaves *Leaf 1* and *Leaf 2* are considered as protostars. B, The dendrogram of the “bar” identified by *astrodendro*.

seen in DCN (fig. S3). The infall rate along the “bar” can be estimated using Eq. 3 which is $2.6 \times 10^{-4} M_{\odot} \text{ yr}^{-1}$, similar to the infall rate of the spiral system.

At the disk scale, assuming the ^{12}CO outflow momentum is conserved from the protostellar wind momentum, we infer the accretion rate \dot{M}_{acc} from the mass-loss rate \dot{M}_{w} estimated from ^{12}CO since \dot{M}_{acc} is proportional to \dot{M}_{w} via $\dot{M}_{\text{acc}} = f \times \dot{M}_{\text{w}}$ (79, 80) where f is the fraction between the accretion rate and mass-loss rate. We estimate the gas mass of the outflow m_i at each channel following (81):

$$m_i = 1.39 \times 10^{-6} \exp\left(\frac{16.59}{T_{\text{ex}}}\right) (T_{\text{ex}} + 0.92) D^2 \int S_i d\Omega, \quad (5)$$

where T_{ex} , D , S_i and Ω are the excitation temperature of ^{12}CO (2-1), the distance in kpc, the flux in Jy of each pixel at channel i , and the solid angle, respectively. Eq. 5 is normalized to a ^{12}CO -to- H_2 abundance of 10^{-4} and a mean gas atomic weight of 1.36. We adopt a T_{ex} of 30 K which is slightly higher than the 20 K used above considering that the gas could be heated by the outflow. The velocity range is free of ^{13}CO and C^{18}O (fig. S12), thus we assume the ^{12}CO emission is optically thin. Measuring the ^{12}CO outflow projection length (λ_{max}), we estimate the outflow dynamical timescale (t_{dyn}), momentum P_{out} , mechanical force F_{out} , and thus mass-loss rate \dot{M}_{w} using:

$$t_{\text{dyn}} = \frac{\lambda_{\text{max}}}{(v_{\text{max,b}} + v_{\text{max,r}})/2}, \quad (6)$$

$$P_{\text{out}} = \sum^{\text{blue}} m_i v_i + \sum^{\text{red}} m_i v_i, \quad (7)$$

$$F_{\text{out}} = P_{\text{out}}/t_{\text{dyn}}, \quad (8)$$

$$\dot{M}_{\text{w}} = \frac{F_{\text{out}}}{v_{\text{w}}}, \quad (9)$$

Here $v_{\text{max,b}}$ and $v_{\text{max,r}}$ are the maximum blueshifted and redshifted ^{12}CO velocities, respectively, and v_w is the wind velocity. We adopt a v_w of 500 km s^{-1} (80, 82). The outflow parameters are summarized in table S2. The mass-loss rates for the blue and red lobes are 5.7 and $3.6 \times 10^{-7} M_{\odot} \text{ yr}^{-1}$, respectively, with a total of $9.3 \times 10^{-7} M_{\odot} \text{ yr}^{-1}$. We adopt the fraction f of 3 (83), resulting in an accretion rate of $2.8 \times 10^{-6} M_{\odot} \text{ yr}^{-1}$.

Table. 1 | Outflow parameters of I18134-1942

Lobe	Δv km s^{-1}	λ_{max} 10^{-3} pc	t_{dyn} 10^3 yr	P_{out} $M_{\odot} \text{ km s}^{-1}$	F_{out} $10^{-2} M_{\odot} \text{ km s}^{-1} \text{ yr}^{-1}$	\dot{M}_w $10^{-5} M_{\odot} \text{ yr}^{-1}$
Blue	[-30,0]	49.91	1.11	26.93	2.42	4.85
Red	[20,50]	18.41	0.41	4.74	1.16	2.31

As we cannot derive the inclination of the outflow, the accretion rate has not been corrected for the projection with a factor of $\cos i / \sin^2 i$. On a hemispherical surface, the probability distribution of the inclination angle i is given by $P(i) \propto \cos i$, where i ranges from 0 to $\pi/2$. The mean inclination angle of the outflow is calculated to be

$$E(i) = \frac{\int_0^{\pi/2} i \cos i \, di}{\int_0^{\pi/2} \cos i \, di} = \frac{\pi}{2} - 1 \text{ radian} \approx 32.7^\circ$$

For the mean inclination angle, the very small (i.e. 5°) and large (i.e. 85°) inclination angle, the correction factors applied to the accretion rate are determined to be 2.9, 131.1, and 0.09, respectively. We estimated the mass inflow rate assuming the inclination of most of the inflows to be 45° . Changing the inclination to 10° or 80° , would increase or reduce the inflow rate by a factor of 5.7. The disk-mediated accretion rate inferred from the outflow would be comparable to the mass inflow rate only under the extreme cases.

References

- [1] J. C. Tan, M. T. Beltrán, P. Caselli, F. Fontani, A. Fuente, M. R. Krumholz, C. F. McKee, and A. Stolte. Massive Star Formation. In Henrik Beuther, Ralf S. Klessen, Cornelis P. Dullemond, and Thomas Henning, editors, *Protostars and Planets VI*, pages 149–172, January 2014. doi: 10.2458/azu_uapress_9780816531240-ch007.
- [2] M. R. Krumholz, M. R. Bate, H. G. Arce, J. E. Dale, R. Gutermuth, R. I. Klein, Z. Y. Li, F. Nakamura, and Q. Zhang. Star Cluster Formation and Feedback. In Henrik Beuther, Ralf S. Klessen, Cornelis P. Dullemond, and Thomas Henning, editors, *Protostars and Planets VI*, pages 243–266, January 2014. doi: 10.2458/azu_uapress_9780816531240-ch011.
- [3] Frédérique Motte, Sylvain Bontemps, and Fabien Louvet. High-Mass Star and Massive Cluster Formation in the Milky Way. *Annu. Rev. Astron. Astrophys.*, 56:41–82, September 2018. doi: 10.1146/annurev-astro-091916-055235.
- [4] Mark R. Krumholz, Christopher F. McKee, and Joss Bland-Hawthorn. Star Clusters Across Cosmic Time. *Annu. Rev. Astron. Astrophys.*, 57:227–303, August 2019. doi: 10.1146/annurev-astro-091918-104430.
- [5] Frank H. Shu, Fred C. Adams, and Susana Lizano. Star formation in molecular clouds: observation and theory. *Annu. Rev. Astron. Astrophys.*, 25:23–81, January 1987. doi: 10.1146/annurev.aa.25.090187.000323.
- [6] Christopher F. McKee and Jonathan C. Tan. The Formation of Massive Stars from Turbulent Cores. *Astrophys. J.*, 585(2):850–871, March 2003. doi: 10.1086/346149.
- [7] T. Csengeri, S. Bontemps, N. Schneider, F. Motte, and S. Dib. Gas dynamics in massive dense cores in Cygnus-X. *Astron. Astrophys.*, 527:A135, March 2011. doi: 10.1051/0004-6361/201014984.
- [8] N. Peretto, G. A. Fuller, A. Duarte-Cabral, A. Avison, P. Hennebelle, J. E. Pineda, Ph. André, S. Bontemps, F. Motte, N. Schneider, and S. Molinari. Global collapse of molecular clouds as a formation mechanism for the most massive stars. *Astron. Astrophys.*, 555: A112, July 2013. doi: 10.1051/0004-6361/201321318.
- [9] Jian-Wen Zhou, Tie Liu, Neal J. Evans, Guido Garay, Paul F. Goldsmith, Gilberto C. Gómez, Enrique Vázquez-Semadeni, Hong-Li Liu, Amelia M. Stutz, Ke Wang, Mika Juvela, Jinhua He, Di Li, Leonardo Bronfman, Xunchuan Liu, Feng-Wei Xu, Anandmayee Tej, L. K. Dewangan, Shanghuo Li, Siju Zhang, Chao Zhang, Zhiyuan Ren, Ken’ichi Tatematsu, Pak Shing Li, Chang Won Lee, Tapas Baug, Sheng-Li Qin, Yuefang Wu, Yaping Peng, Yong Zhang, Rong Liu, Qiu-Yi Luo, Jixing Ge, Anindya Saha, Eswaraiah Chakali, Qizhou Zhang, Kee-Tae Kim, Isabelle Ristorcelli, Zhi-Qiang Shen, and Jin-Zeng Li. ATOMS: ALMA Three-millimeter Observations of Massive Star-forming regions - XI. From inflow to infall in hub-filament systems. *Mon. Not. R. Astron. Soc.*, 514(4): 6038–6052, August 2022. doi: 10.1093/mnras/stac1735.
- [10] J. W. Zhou, S. Dib, M. Juvela, P. Sanhueza, F. Wyrowski, T. Liu, and K. M. Menten. Gas inflows from cloud to core scales in G332.83-0.55: Hierarchical hub-filament structures and tide-regulated gravitational collapse. *Astron. Astrophys.*, 686:A146, June 2024. doi: 10.1051/0004-6361/202449514.

- [11] M. T. Beltrán and W. J. de Wit. Accretion disks in luminous young stellar objects. *Astron. Astrophys. Rev.*, 24:6, January 2016. doi: 10.1007/s00159-015-0089-z.
- [12] Yichen Zhang, Jonathan C. Tan, Kei E. I. Tanaka, James M. De Buizer, Mengyao Liu, Maria T. Beltrán, Kaitlin Kratter, Diego Mardones, and Guido Garay. Dynamics of a massive binary at birth. *Nature Astronomy*, 3:517–523, March 2019. doi: 10.1038/s41550-019-0718-y.
- [13] Xing Lu, Guang-Xing Li, Qizhou Zhang, and Yuxin Lin. A massive Keplerian protostellar disk with flyby-induced spirals in the Central Molecular Zone. *Nature Astronomy*, 6:837–843, May 2022. doi: 10.1038/s41550-022-01681-4.
- [14] A. Caratti o Garatti, B. Stecklum, R. Garcia Lopez, J. Eislöffel, T. P. Ray, A. Sanna, R. Cesaroni, C. M. Walmsley, R. D. Oudmaijer, W. J. de Wit, L. Moscadelli, J. Greiner, A. Krabbe, C. Fischer, R. Klein, and J. M. Ibañez. Disk-mediated accretion burst in a high-mass young stellar object. *Nature Physics*, 13(3):276–279, March 2017. doi: 10.1038/nphys3942.
- [15] Fernando A. Olguin, Patricio Sanhueza, Huei-Ru Vivien Chen, Xing Lu, Yoko Oya, Qizhou Zhang, Adam Ginsburg, Kotomi Taniguchi, Shanghuo Li, Kaho Morii, Takeshi Sakai, and Fumitaka Nakamura. Digging into the Interior of Hot Cores with ALMA: Spiral Accretion into the High-mass Protostellar Core G336.01-0.82. *Astrophys. J. Lett.*, 959(2):L31, December 2023. doi: 10.3847/2041-8213/ad1100.
- [16] Anna F. McLeod, Pamela D. Klaassen, Megan Reiter, Jonathan Henshaw, Rolf Kuiper, and Adam Ginsburg. A probable Keplerian disk feeding an optically revealed massive young star. *Nature*, 625(7993):55–59, January 2024. doi: 10.1038/s41586-023-06790-2.
- [17] Y. W. Wu, M. Sato, M. J. Reid, L. Moscadelli, B. Zhang, Y. Xu, A. Brunthaler, K. M. Menten, T. M. Dame, and X. W. Zheng. Trigonometric parallaxes of star-forming regions in the Sagittarius spiral arm. *Astron. Astrophys.*, 566:A17, June 2014. doi: 10.1051/0004-6361/201322765.
- [18] D. J. van der Walt, E. Churchwell, M. J. Gaylard, and S. Goedhart. Radio continuum emission associated with Class II methanol maser sources. *Mon. Not. R. Astron. Soc.*, 341(1):270–276, May 2003. doi: 10.1046/j.1365-8711.2003.06416.x.
- [19] J. S. Urquhart, C. König, A. Giannetti, S. Leurini, T. J. T. Moore, D. J. Eden, T. Pillai, M. A. Thompson, C. Braiding, M. G. Burton, T. Csengeri, J. T. Dempsey, C. Figura, D. Froebrich, K. M. Menten, F. Schuller, M. D. Smith, and F. Wyrowski. ATLASGAL - properties of a complete sample of Galactic clumps. *Mon. Not. R. Astron. Soc.*, 473(1): 1059–1102, January 2018. doi: 10.1093/mnras/stx2258.
- [20] A. J. Schutte, D. J. van der Walt, M. J. Gaylard, and G. C. MacLeod. Detection of 35 new 5 1 -6 0 A+ -methanol masers towards IRAS sources. *Mon. Not. R. Astron. Soc.*, 261: 783–794, April 1993. doi: 10.1093/mnras/261.4.783.
- [21] M. R. Pestalozzi, V. Minier, and R. S. Booth. A general catalogue of 6.7-GHz methanol masers. I. Data. *Astron. Astrophys.*, 432(2):737–742, March 2005. doi: 10.1051/0004-6361:20035855.

- [22] F. Fontani, R. Cesaroni, and R. S. Furuya. Class I and Class II methanol masers in high-mass star-forming regions. *Astron. Astrophys.*, 517:A56, July 2010. doi: 10.1051/0004-6361/200913679.
- [23] M. Szymczak and A. J. Kus. A survey of the 6.7 GHz methanol maser emission from IRAS sources — II. Statistical analysis. *Astron. Astrophys.*, 360:311–318, August 2000.
- [24] John Galt. Spectra of Star Formation Regions at the 6.7 GHz Methanol Line. *Astron. J.*, 127(6):3479–3483, June 2004. doi: 10.1086/420713.
- [25] O. S. Bayandina, R. A. Burns, A. Caratti o Garatti, S. E. Kurtz, L. Moscadelli, N. N. Shakhvorostova, A. M. Sobolev, Y. Tanabe, I. E. Val’tts, and Y. Yonekura. Star formation in G11.497-1.485: Two-epoch VLA study of a 6.7 GHz methanol maser flare. *Astron. Astrophys.*, 684:A86, April 2024. doi: 10.1051/0004-6361/202348656.
- [26] F. Palla, J. Brand, R. Cesaroni, G. Comoretto, and M. Felli. Water masers associated with dense molecular clouds and ultracompact HII regions. *Astron. Astrophys.*, 246:249–263, June 1991.
- [27] Kazuyoshi Sunada, Takeshi Nakazato, Norio Ikeda, Satoshi Hongo, Yoshimi Kitamura, and Ji Yang. Water Maser and Ammonia Survey toward IRAS Sources in the Galaxy I. H₂O Maser Data. *Publ. Astron. Soc. Jpn.*, 59:1185, December 2007. doi: 10.1093/pasj/59.6.1185.
- [28] C. Codella, M. Felli, and V. Natale. The occurrence of H₂O masers in the early stages of star formation. *Astron. Astrophys.*, 311:971–980, July 1996.
- [29] S. L. Breen, J. L. Caswell, S. P. Ellingsen, and C. J. Phillips. Water masers accompanying OH and methanol masers in star formation regions. *Mon. Not. R. Astron. Soc.*, 406(3): 1487–1532, August 2010. doi: 10.1111/j.1365-2966.2010.16791.x.
- [30] Chin-Fei Lee, Zhi-Yun Li, and Neal J. Turner. Spiral structures in an embedded proto-stellar disk driven by envelope accretion. *Nature Astronomy*, 4:142–146, February 2020. doi: 10.1038/s41550-019-0905-x.
- [31] Xi Chen, Andrej M. Sobolev, Zhi-Yuan Ren, Sergey Parfenov, Shari L. Breen, Simon P. Ellingsen, Zhi-Qiang Shen, Bin Li, Gordon C. MacLeod, Willem Baan, Crystal Brogan, Tomoya Hirota, Todd R. Hunter, Hendrik Linz, Karl Menten, Koichiro Sugiyama, Bringfried Stecklum, Yan Gong, and Xingwu Zheng. New maser species tracing spiral-arm accretion flows in a high-mass young stellar object. *Nature Astronomy*, 4:1170–1176, January 2020. doi: 10.1038/s41550-020-1144-x.
- [32] R. A. Burns, Y. Uno, N. Sakai, J. Blanchard, Z. Rosli, G. Orosz, Y. Yonekura, Y. Tanabe, K. Sugiyama, T. Hirota, Kee-Tae Kim, A. Aberfelds, A. E. Volvach, A. Bartkiewicz, A. Caratti o Garatti, A. M. Sobolev, B. Stecklum, C. Brogan, C. Phillips, D. A. Ladeyschikov, D. Johnstone, G. Surcis, G. C. MacLeod, H. Linz, J. O. Chibueze, J. Brand, J. Eislöffel, L. Hyland, L. Uscanga, M. Olech, M. Durjasz, O. Bayandina, S. Breen, S. P. Ellingsen, S. P. van den Heever, T. R. Hunter, and X. Chen. A Keplerian disk with a four-arm spiral birthing an episodically accreting high-mass protostar. *Nature Astronomy*, 7: 557–568, May 2023. doi: 10.1038/s41550-023-01899-w.

- [33] Jessica Speedie, Ruobing Dong, Cassandra Hall, Cristiano Longarini, Benedetta Veronesi, Teresa Paneque-Carreño, Giuseppe Lodato, Ya-Wen Tang, Richard Teague, and Jun Hashimoto. Gravitational instability in a planet-forming disk. *Nature*, 633(8028):58–62, September 2024. doi: 10.1038/s41586-024-07877-0.
- [34] Haoyu Baobab Liu, Roberto Galván-Madrid, Izaskun Jiménez-Serra, Carlos Román-Zúñiga, Qizhou Zhang, Zhiyun Li, and Huei-Ru Chen. ALMA Resolves the Spiraling Accretion Flow in the Luminous OB Cluster-forming Region G33.92+0.11. *Astrophys. J.*, 804(1):37, May 2015. doi: 10.1088/0004-637X/804/1/37.
- [35] Patricio Sanhueza, Josep Miquel Girart, Marco Padovani, Daniele Galli, Charles L. H. Hull, Qizhou Zhang, Paulo Cortes, Ian W. Stephens, Manuel Fernández-López, James M. Jackson, Pau Frau, Patrick M. Kock, Benjamin Wu, Luis A. Zapata, Fernando Olguin, Xing Lu, Andrea Silva, Ya-Wen Tang, Takeshi Sakai, Andrés E. Guzmán, Ken’ichi Tatematsu, Fumitaka Nakamura, and Huei-Ru Vivien Chen. Gravity-driven Magnetic Field at 1000 au Scales in High-mass Star Formation. *Astrophys. J. Lett.*, 915(1):L10, July 2021. doi: 10.3847/2041-8213/ac081c.
- [36] Jihye Hwang, Jongsoo Kim, Kate Pattle, Chang Won Lee, Patrick M. Koch, Doug Johnstone, Kohji Tomisaka, Anthony Whitworth, Ray S. Furuya, Ji-hyun Kang, A. Ran Lyo, Eun Jung Chung, Doris Arzoumanian, Geumsook Park, Woojin Kwon, Shinyoung Kim, Motohide Tamura, Jungmi Kwon, Archana Soam, Ilseung Han, Thiem Hoang, Kyoung Hee Kim, Takashi Onaka, Chakali Eswaraiah, Derek Ward-Thompson, Hong-Li Liu, Xindi Tang, Wen Ping Chen, Masafumi Matsumura, Thuong Duc Hoang, Zhiwei Chen, Valentin J. M. Le Gouellec, Florian Kirchschrager, Frédérick Poidevin, Pierre Bastien, Keping Qiu, Tetsuo Hasegawa, Shih-Ping Lai, Do-Young Byun, Jungyeon Cho, Minhoo Choi, Youngwoo Choi, Yunhee Choi, Il-Gyo Jeong, Miju Kang, Hyosung Kim, Kee-Tae Kim, Jeong-Eun Lee, Sang-Sung Lee, Yong-Hee Lee, Hyeeseung Lee, Mi-Ryang Kim, Hyunju Yoo, Hyeong-Sik Yun, Mike Chen, James Di Francesco, Jason Fiege, Laura M. Fissel, Erica Franzmann, Martin Houde, Kevin Lacaille, Brenda Matthews, Sarah Sadavoy, Gerald Moriarty-Schieven, Mehrnoosh Tahani, Tao-Chung Ching, Y. Sophia Dai, Yan Duan, Qilao Gu, Chi-Yan Law, Dalei Li, Di Li, Guangxing Li, Hua-bai Li, Tie Liu, Xing Lu, Lei Qian, Hongchi Wang, Jintai Wu, Jinjin Xie, Jinghua Yuan, Chuan-Peng Zhang, Guoyin Zhang, Yapeng Zhang, Jianjun Zhou, Lei Zhu, David Berry, Per Friberg, Sarah Graves, Junhao Liu, Steve Mairs, Harriet Parsons, Mark Rawlings, Yasuo Doi, Saeko Hayashi, Charles L. H. Hull, Tsuyoshi Inoue, Shu-ichiro Inutsuka, Kazunari Iwasaki, Akimasa Kataoka, Koji Kawabata, Gwanjeong Kim, Masato I. N. Kobayashi, Tetsuya Nagata, Fumitaka Nakamura, Hiroyuki Nakanishi, Tae-Soo Pyo, Hiro Saito, Masumichi Seta, Yoshito Shimajiri, Hiroko Shinnaga, Yusuke Tsukamoto, Tetsuya Zenko, Huei-Ru Vivien Chen, Hao-Yuan Duan, Lapo Fanciullo, Francisca Kemper, Chin-Fei Lee, Sheng-Jun Lin, Sheng-Yuan Liu, Nagayoshi Ohashi, Ramprasad Rao, Ya-Wen Tang, Jia-Wei Wang, Meng-Zhe Yang, Hsi-Wei Yen, Tyler L. Bourke, Antonio Chrysostomou, Victor Debattista, David Eden, Stewart Eyres, Sam Falle, Gary Fuller, Tim Gledhill, Jane Greaves, Matt Griffin, Jennifer Hatchell, Janik Karoly, Jason Kirk, Vera Könyves, Steven Longmore, Sven van Loo, Ilse de Looze, Nicolas Peretto, Felix Priestley, Jonathan Rawlings, Brendan Retter, John Richer, Andrew Rigby, Giorgio Savini, Anna Scaife, Serena Viti, Pham Ngoc Diep, Nguyen Bich Ngoc, Le Ngoc Tram, Philippe André, Simon Coudé, C. Darren Dowell, Rachel Friesen, and Jean-François Robitaille. The JCMT BISTRO Sur-

- vey: A Spiral Magnetic Field in a Hub-filament Structure, Monoceros R2. *Astrophys. J.*, 941(1):51, December 2022. doi: 10.3847/1538-4357/ac99e0.
- [37] Feng-Wei Xu, Ke Wang, Tie Liu, Paul F. Goldsmith, Qizhou Zhang, Mika Juvela, Hong-Li Liu, Sheng-Li Qin, Guang-Xing Li, Anandmayee Tej, Guido Garay, Leonardo Bronfman, Shanghuo Li, Yue-Fang Wu, Gilberto C. Gómez, Enrique Vázquez-Semadeni, Ken'ichi Tatematsu, Zhiyuan Ren, Yong Zhang, L. Viktor Toth, Xunchuan Liu, Nannan Yue, Siju Zhang, Tapas Baug, Namitha Issac, Amelia M. Stutz, Meizhu Liu, Gary A. Fuller, Mengyao Tang, Chao Zhang, Lokesh Dewangan, Chang Won Lee, Jianwen Zhou, Jinjin Xie, Wenyu Jiao, Chao Wang, Rong Liu, Qiuyi Luo, Archana Soam, and Chakali Eswaraiah. ATOMS: ALMA Three-millimeter Observations of Massive Star-forming regions - XV. Steady accretion from global collapse to core feeding in massive hub-filament system SDC335. *Mon. Not. R. Astron. Soc.*, 520(3):3259–3285, April 2023. doi: 10.1093/mnras/stad012.
- [38] Mavis Seidu, J. O. Chibueze, Gary A. Fuller, A. Avison, and N. Asabre Frimpong. MeerKAT and ALMA view of the AGAL045.804 - 0.356 clump. *Mon. Not. R. Astron. Soc.*, 530(2):1956–1967, May 2024. doi: 10.1093/mnras/stae987.
- [39] S. Mendoza, E. Tejeda, and E. Nagel. Analytic solutions to the accretion of a rotating finite cloud towards a central object - I. Newtonian approach. *Mon. Not. R. Astron. Soc.*, 393(2):579–586, February 2009. doi: 10.1111/j.1365-2966.2008.14210.x.
- [40] Jaime E. Pineda, Dominique Segura-Cox, Paola Caselli, Nichol Cunningham, Bo Zhao, Anika Schmiedeke, María José Maureira, and Roberto Neri. A protostellar system fed by a streamer of 10,500 au length. *Nature Astronomy*, 4:1158–1163, January 2020. doi: 10.1038/s41550-020-1150-z.
- [41] Xing Lu, Qizhou Zhang, Haoyu Baobab Liu, Patricio Sanhueza, Ken'ichi Tatematsu, Siyi Feng, Howard A. Smith, Philip C. Myers, T. K. Sridharan, and Qiusheng Gu. Filamentary Fragmentation and Accretion in High-mass Star-forming Molecular Clouds. *Astrophys. J.*, 855(1):9, March 2018. doi: 10.3847/1538-4357/aaad11.
- [42] Elena Redaelli, Stefano Bovino, Patricio Sanhueza, Kaho Morii, Giovanni Sabatini, Paola Caselli, Andrea Giannetti, and Shanghuo Li. The Core Population and Kinematics of a Massive Clump at Early Stages: An Atacama Large Millimeter/submillimeter Array View. *Astrophys. J.*, 936(2):169, September 2022. doi: 10.3847/1538-4357/ac85b4.
- [43] S. Zhang, C. J. Cyganowski, J. D. Henshaw, C. L. Brogan, T. R. Hunter, R. K. Friesen, I. A. Bonnell, and S. Viti. Filamentary mass accretion towards the high-mass protobinary system G11.92-0.61 MM2. *Mon. Not. R. Astron. Soc.*, 533(1):1075–1094, September 2024. doi: 10.1093/mnras/stae1844.
- [44] Nami Sakai, Yoko Oya, Takeshi Sakai, Yoshimasa Watanabe, Tomoya Hirota, Cecilia Ceccarelli, Claudine Kahane, Ana Lopez-Sepulcre, Bertrand Lefloch, Charlotte Vastel, Sandrine Bottinelli, Emmanuel Caux, Audrey Coutens, Yuri Aikawa, Shigehisa Takakuwa, Nagayoshi Ohashi, Hsi-Wei Yen, and Satoshi Yamamoto. A Chemical View of Protostellar-disk Formation in L1527. *Astrophys. J. Lett.*, 791(2):L38, August 2014. doi: 10.1088/2041-8205/791/2/L38.

- [45] Yoko Oya, Nami Sakai, Bertrand Lefloch, Ana López-Sepulcre, Yoshimasa Watanabe, Cecilia Ceccarelli, and Satoshi Yamamoto. Geometric and Kinematic Structure of the Outflow/Envelope System of L1527 Revealed by Subarcsecond-resolution Observation of CS. *Astrophys. J.*, 812(1):59, October 2015. doi: 10.1088/0004-637X/812/1/59.
- [46] Yoko Oya, Nami Sakai, Ana López-Sepulcre, Yoshimasa Watanabe, Cecilia Ceccarelli, Bertrand Lefloch, Cécile Favre, and Satoshi Yamamoto. Infalling-Rotating Motion and Associated Chemical Change in the Envelope of IRAS 16293-2422 Source A Studied with ALMA. *Astrophys. J.*, 824(2):88, June 2016. doi: 10.3847/0004-637X/824/2/88.
- [47] Yoko Oya, Nami Sakai, Yoshimasa Watanabe, Aya E. Higuchi, Tomoya Hirota, Ana López-Sepulcre, Takeshi Sakai, Yuri Aikawa, Cecilia Ceccarelli, Bertrand Lefloch, Emmanuel Caux, Charlotte Vastel, Claudine Kahane, and Satoshi Yamamoto. L483: Warm Carbon-chain Chemistry Source Harboring Hot Corino Activity. *Astrophys. J.*, 837(2): 174, March 2017. doi: 10.3847/1538-4357/aa6300.
- [48] Yichen Zhang, Jonathan C. Tan, Nami Sakai, Kei E. I. Tanaka, James M. De Buizer, Mengyao Liu, Maria T. Beltrán, Kaitlin Kratter, Diego Mardones, and Guido Garay. An Ordered Envelope-Disk Transition in the Massive Protostellar Source G339.88-1.26. *Astrophys. J.*, 873(1):73, March 2019. doi: 10.3847/1538-4357/ab0553.
- [49] Satoshi Ohashi, Claudio Codella, Nami Sakai, Claire J. Chandler, Cecilia Ceccarelli, Felipe Alves, Davide Fedele, Tomoyuki Hanawa, Aurora Durán, Cécile Favre, Ana López-Sepulcre, Laurent Loinard, Seyma Mercimek, Nadia M. Murillo, Linda Podio, Yichen Zhang, Yuri Aikawa, Nadia Balucani, Eleonora Bianchi, Mathilde Bouvier, Gemma Busquet, Paola Caselli, Emmanuel Caux, Steven Charnley, Spandan Choudhury, Nicolas Cuello, Marta De Simone, Francois Dulieu, Lucy Evans, Siyi Feng, Francesco Fontani, Logan Francis, Tetsuya Hama, Eric Herbst, Shingo Hirano, Tomoya Hirota, Muneaki Imai, Andrea Isella, Izaskun Jiménez-Serra, Doug Johnstone, Claudine Kahane, Romane Le Gal, Bertrand Lefloch, Luke T. Maud, Maria Jose Maureira, Francois Menard, Anna Miotello, George Moellenbrock, Shoji Mori, Rieuhei Nakatani, Hideko Nomura, Yasuhiro Oba, Ross O'Donoghue, Yuki Okoda, Juan Ospina-Zamudio, Yoko Oya, Jaime Pineda, Albert Rimola, Takeshi Sakai, Dominique Segura-Cox, Yancy Shirley, Brian Svoboda, Vianney Taquet, Leonardo Testi, Charlotte Vastel, Serena Viti, Naoki Watanabe, Yoshimasa Watanabe, Arezu Witzel, Ci Xue, Bo Zhao, and Satoshi Yamamoto. Misaligned Rotations of the Envelope, Outflow, and Disks in the Multiple Protostellar System of VLA 1623-2417: FAUST. III. *Astrophys. J.*, 927(1):54, March 2022. doi: 10.3847/1538-4357/ac4cae.
- [50] C. Brinch, A. Crapsi, J. K. Jørgensen, M. R. Hogerheijde, and T. Hill. A deeply embedded young protoplanetary disk around L1489 IRS observed by the Submillimeter Array. *Astron. Astrophys.*, 475(3):915–923, December 2007. doi: 10.1051/0004-6361:20078249.
- [51] C. Brinch, A. Crapsi, M. R. Hogerheijde, and J. K. Jørgensen. Structure and dynamics of the class I young stellar object L1489 IRS. *Astron. Astrophys.*, 461(3):1037–1047, January 2007. doi: 10.1051/0004-6361:20065473.
- [52] Daisuke Takaishi, Yusuke Tsukamoto, and Yasushi Suto. A new formation scenario of a counter-rotating circumstellar disk: Spiral-arm accretion from a circumbinary disk in

- a triple protostar system. *Publ. Astron. Soc. Jpn.*, 73(5):L25–L30, October 2021. doi: 10.1093/pasj/psab084.
- [53] Zhi-Yun Li, Ruben Krasnopolsky, and Hsien Shang. Non-ideal MHD Effects and Magnetic Braking Catastrophe in Protostellar Disk Formation. *Astrophys. J.*, 738(2):180, September 2011. doi: 10.1088/0004-637X/738/2/180.
 - [54] Yusuke Tsukamoto, Satoshi Okuzumi, Kazunari Iwasaki, Masahiro N. Machida, and Shu-ichiro Inutsuka. The impact of the Hall effect during cloud core collapse: Implications for circumstellar disk evolution. *Publ. Astron. Soc. Jpn.*, 69(6):95, December 2017. doi: 10.1093/pasj/psx113.
 - [55] Tomoaki Matsumoto, Masahiro N. Machida, and Shu-ichiro Inutsuka. Circumstellar Disks and Outflows in Turbulent Molecular Cloud Cores: Possible Formation Mechanism for Misaligned Systems. *Astrophys. J.*, 839(1):69, April 2017. doi: 10.3847/1538-4357/aa6a1c.
 - [56] Veli-Matti Pelkonen, Paolo Padoan, Mika Juvela, Troels Haugbølle, and Åke Nordlund. Origin and Evolution of Angular Momentum of Class II Disks. *arXiv e-prints*, art. arXiv:2405.06520, May 2024. doi: 10.48550/arXiv.2405.06520.
 - [57] Mark J. Pecaut and Eric E. Mamajek. Intrinsic Colors, Temperatures, and Bolometric Corrections of Pre-main-sequence Stars. *Astrophys. J. Suppl. Ser.*, 208(1):9, September 2013. doi: 10.1088/0067-0049/208/1/9.
 - [58] M. Kuffmeier, C. P. Dullemond, S. Reissl, and F. G. Goicovic. Misaligned disks induced by infall. *Astron. Astrophys.*, 656:A161, December 2021. doi: 10.1051/0004-6361/202039614.
 - [59] Shanghuo Li, Patricio Sanhueza, Qizhou Zhang, Fumitaka Nakamura, Xing Lu, Junzhi Wang, Tie Liu, Ken’ichi Tatematsu, James M. Jackson, Andrea Silva, Andrés E. Guzmán, Takeshi Sakai, Natsuko Izumi, Daniel Tafuya, Fei Li, Yanett Contreras, Kaho Morii, and Kee-Tae Kim. The ALMA Survey of 70 μ m Dark High-mass Clumps in Early Stages (ASHES). II. Molecular Outflows in the Extreme Early Stages of Protocluster Formation. *Astrophys. J.*, 903(2):119, November 2020. doi: 10.3847/1538-4357/abb81f.
 - [60] Giseon Baek, Jeong-Eun Lee, Neal J. Evans, Tomoya Hirota, Yuri Aikawa, Ji-hyun Kang, Jungha Kim, and Jes K. Jørgensen. Spectral Survey of a Hot Core with an Eruptive Accretion in S255IR NIRS3 (SHEA): The Discovery of Class I and II Millimeter Methanol Maser Transitions. *Astrophys. J. Lett.*, 954(1):L25, September 2023. doi: 10.3847/2041-8213/acef1d.
 - [61] Jeong-Eun Lee, Chul-Hwan Kim, Seokho Lee, Seonjae Lee, Giseon Baek, Hyeong-Sik Yun, Yuri Aikawa, Doug Johnstone, Gregory J. Herczeg, and Lucas Cieza. ALMA Spectral Survey of an Eruptive Young Star, V883 Ori (ASSAY). I. What Triggered the Current Episode of Eruption? *Astrophys. J.*, 966(1):119, May 2024. doi: 10.3847/1538-4357/ad3106.
 - [62] Thor Tepper-García, Joss Bland-Hawthorn, Eugene Vasiliev, Oscar Agertz, Romain Teyssier, and Christoph Federrath. NEXUS: a framework for controlled simulations of idealized galaxies. *Mon. Not. R. Astron. Soc.*, 535(1):187–206, November 2024. doi: 10.1093/mnras/stae2372.

- [63] Joss Bland-Hawthorn, Thor Tepper-Garcia, Oscar Agertz, and Christoph Federrath. Turbulent Gas-rich Disks at High Redshift: Bars and Bulges in a Radial Shear Flow. *Astrophys. J.*, 968(2):86, June 2024. doi: 10.3847/1538-4357/ad4118.
- [64] Joss Bland-Hawthorn, Thor Tepper-Garcia, Oscar Agertz, Christoph Federrath, Misha Haywood, Paola di Matteo, Timothy R Bedding, Takafumi Tsukui, Emily Wisnioski, Melissa Ness, and Ken Freeman. Turbulent gas-rich discs at high redshift: origin of thick stellar discs through 3D 'baryon sloshing'. *arXiv e-prints*, art. arXiv:2502.01895, February 2025. doi: 10.48550/arXiv.2502.01895.
- [65] J. M. De Buizer. Testing the circumstellar disc hypothesis: a search for H₂ outflow signatures from massive young stellar objects with linearly distributed methanol masers. *Monthly Notices of the Royal Astronomical Society*, 341(1):277–298, 05 2003. ISSN 0035-8711. doi: 10.1046/j.1365-8711.2003.06419.x. URL <https://doi.org/10.1046/j.1365-8711.2003.06419.x>.
- [66] S. Claude, F. Jiang, P. Niranjana, P. Dindo, D. Erickson, K. Yeung, D. Derdall, D. Duncan, D. Garcia, B. Leckie, M. Pflieger, G. Rodrigues, K. Szeto, P. Welle, I. Wood, K. Caputa, A. Lichtenberger, and S. K. Pan. Performance of the pre-production band 3 (84–116 GHz) receivers for ALMA. In William D. Duncan, Wayne S. Holland, Stafford Withington, and Jonas Zmuidzinas, editors, *Millimeter and Submillimeter Detectors and Instrumentation for Astronomy IV*, volume 7020 of *Society of Photo-Optical Instrumentation Engineers (SPIE) Conference Series*, page 70201B, July 2008. doi: 10.1117/12.788128.
- [67] J. P. McMullin, B. Waters, D. Schiebel, W. Young, and K. Golap. CASA Architecture and Applications. In R. A. Shaw, F. Hill, and D. J. Bell, editors, *Astronomical Data Analysis Software and Systems XVI*, volume 376 of *Astronomical Society of the Pacific Conference Series*, page 127, October 2007.
- [68] Tie Liu, Neal J. Evans, Kee-Tae Kim, Paul F. Goldsmith, Sheng-Yuan Liu, Qizhou Zhang, Ken'ichi Tatematsu, Ke Wang, Mika Juvela, Leonardo Bronfman, Maria R. Cunningham, Guido Garay, Tomoya Hirota, Jeong-Eun Lee, Sung-Ju Kang, Di Li, Pak-Shing Li, Diego Mardones, Sheng-Li Qin, Isabelle Ristorcelli, Anandmayee Tej, L. Viktor Toth, Jing-Wen Wu, Yue-Fang Wu, Hee-weon Yi, Hyeong-Sik Yun, Hong-Li Liu, Ya-Ping Peng, Juan Li, Shang-Huo Li, Chang Won Lee, Zhi-Qiang Shen, Tapas Baug, Jun-Zhi Wang, Yong Zhang, Namitha Issac, Feng-Yao Zhu, Qiu-Yi Luo, Archana Soam, Xun-Chuan Liu, Feng-Wei Xu, Yu Wang, Chao Zhang, Zhiyuan Ren, and Chao Zhang. ATOMS: ALMA Three-millimeter Observations of Massive Star-forming regions - I. Survey description and a first look at G9.62+0.19. *Mon. Not. R. Astron. Soc.*, 496(3):2790–2820, August 2020. doi: 10.1093/mnras/staa1577.
- [69] G. A. Ediss, M. Carter, J. Cheng, J. E. Effland, W. Grammer, Jr. Horner, N., A. R. Kerr, D. Koller, E. F. Lauria, G. Morris, S. K. Pan, G. Reiland, and M. Sullivan. ALMA Band 6 Cartridge: Design and Performance. In Gopal Narayanan, editor, *Fifteenth International Symposium on Space Terahertz Technology*, pages 181–188, January 2004.
- [70] Xunchuan Liu, Tie Liu, Lei Zhu, Guido Garay, Hong-Li Liu, Paul Goldsmith, Neal Evans, Kee-Tae Kim, Sheng-Yuan Liu, Fengwei Xu, Xing Lu, Anandmayee Tej, Xiaofeng Mai, Leonardo Bronfman, Shanghuo Li, Diego Mardones, Amelia Stutz, Ken'ichi

- Tatematsu, Ke Wang, Qizhou Zhang, Sheng-Li Qin, Jianwen Zhou, Qiuyi Luo, Siju Zhang, Yu Cheng, Jinhua He, Qilao Gu, Ziyang Li, Zhenying Zhang, Suinan Zhang, Anindya Saha, Lokesh Dewangan, Patricio Sanhueza, and Zhiqiang Shen. The ALMA-QUARKS Survey. I. Survey Description and Data Reduction. Research in Astronomy and Astrophysics, 24(2):025009, February 2024. doi: 10.1088/1674-4527/ad0d5c.
- [71] Yoko Oya, Hirofumi Kibukawa, Shota Miyake, and Satoshi Yamamoto. FERIA: Flat Envelope Model with Rotation and Infall under Angular Momentum Conservation. Publ. Astron. Soc. Pac., 134(1039):094301, September 2022. doi: 10.1088/1538-3873/ac8839.
- [72] Jeffrey G. Mangum and Yancy L. Shirley. How to Calculate Molecular Column Density. Publ. Astron. Soc. Pac., 127(949):266, March 2015. doi: 10.1086/680323.
- [73] H. S. P. Müller, S. Thorwirth, D. A. Roth, and G. Winnewisser. The Cologne Database for Molecular Spectroscopy, CDMS. Astron. Astrophys., 370:L49–L52, April 2001. doi: 10.1051/0004-6361:20010367.
- [74] Sadia Hoq, James M. Jackson, Jonathan B. Foster, Patricio Sanhueza, Andrés Guzmán, J. Scott Whitaker, Christopher Claysmith, Jill M. Rathborne, Tatiana Vasyunina, and Anton Vasyunin. Chemical Evolution in High-mass Star-forming Regions: Results from the MALT90 Survey. Astrophys. J., 777(2):157, November 2013. doi: 10.1088/0004-637X/777/2/157.
- [75] Patricio Sanhueza, James M. Jackson, Jonathan B. Foster, Guido Garay, Andrea Silva, and Susanna C. Finn. Chemistry in Infrared Dark Cloud Clumps: A Molecular Line Survey at 3 mm. Astrophys. J., 756(1):60, September 2012. doi: 10.1088/0004-637X/756/1/60.
- [76] Helen Kirk, Philip C. Myers, Tyler L. Bourke, Robert A. Gutermuth, Abigail Hedden, and Grant W. Wilson. Filamentary Accretion Flows in the Embedded Serpens South Protocluster. Astrophys. J., 766(2):115, April 2013. doi: 10.1088/0004-637X/766/2/115.
- [77] E. W. Rosolowsky, J. E. Pineda, J. Kauffmann, and A. A. Goodman. Structural Analysis of Molecular Clouds: Dendrograms. Astrophys. J., 679(2):1338–1351, June 2008. doi: 10.1086/587685.
- [78] V. Ossenkopf and Th. Henning. Dust opacities for protostellar cores. Astron. Astrophys., 291:943–959, November 1994.
- [79] L. E. Ellerbroek, L. Podio, L. Kaper, H. Sana, D. Huppenkothen, A. de Koter, and L. Monaco. The outflow history of two Herbig-Haro jets in RCW 36: HH 1042 and HH 1043. Astron. Astrophys., 551:A5, March 2013. doi: 10.1051/0004-6361/201220635.
- [80] John Bally. Protostellar Outflows. Annu. Rev. Astron. Astrophys., 54:491–528, September 2016. doi: 10.1146/annurev-astro-081915-023341.
- [81] Keping Qiu, Qizhou Zhang, Jingwen Wu, and Huei-Ru Chen. Submillimeter Array Observations of the Molecular Outflow in High-Mass Star-Forming Region G240.31+0.07. Astrophys. J., 696(1):66–74, May 2009. doi: 10.1088/0004-637X/696/1/66.
- [82] Henny J. G. L. M. Lamers, Theodore P. Snow, and Douglas M. Lindholm. Terminal Velocities and the Bistability of Stellar Winds. Astrophys. J., 455:269, December 1995. doi: 10.1086/176575.

- [83] Kohji Tomisaka. Collapse-Driven Outflow in Star-Forming Molecular Cores. *Astrophys. J. Lett.*, 502(2):L163–L167, August 1998. doi: 10.1086/311504.
- [84] Charles R. Harris, K. Jarrod Millman, Stéfan J. van der Walt, Ralf Gommers, Pauli Virtanen, David Cournapeau, Eric Wieser, Julian Taylor, Sebastian Berg, Nathaniel J. Smith, Robert Kern, Matti Picus, Stephan Hoyer, Marten H. van Kerkwijk, Matthew Brett, Allan Haldane, Jaime Fernández del Río, Mark Wiebe, Pearu Peterson, Pierre Gérard-Marchant, Kevin Sheppard, Tyler Reddy, Warren Weckesser, Hameer Abbasi, Christoph Gohlke, and Travis E. Oliphant. Array programming with NumPy. *Nature*, 585(7825):357–362, September 2020. doi: 10.1038/s41586-020-2649-2. URL <https://doi.org/10.1038/s41586-020-2649-2>.
- [85] Pauli Virtanen, Ralf Gommers, Travis E. Oliphant, Matt Haberland, Tyler Reddy, David Cournapeau, Evgeni Burovski, Pearu Peterson, Warren Weckesser, Jonathan Bright, Stéfan J. van der Walt, Matthew Brett, Joshua Wilson, K. Jarrod Millman, Nikolay Mayorov, Andrew R. J. Nelson, Eric Jones, Robert Kern, Eric Larson, C J Carey, İlhan Polat, Yu Feng, Eric W. Moore, Jake VanderPlas, Denis Laxalde, Josef Perktold, Robert Cimrman, Ian Henriksen, E. A. Quintero, Charles R. Harris, Anne M. Archibald, Antônio H. Ribeiro, Fabian Pedregosa, Paul van Mulbregt, and SciPy 1.0 Contributors. SciPy 1.0: Fundamental Algorithms for Scientific Computing in Python. *Nature Methods*, 17:261–272, 2020. doi: 10.1038/s41592-019-0686-2.
- [86] Astropy Collaboration, Thomas P. Robitaille, Erik J. Tollerud, Perry Greenfield, Michael Droettboom, Erik Bray, Tom Aldcroft, Matt Davis, Adam Ginsburg, Adrian M. Price-Whelan, Wolfgang E. Kerzendorf, Alexander Conley, Neil Crighton, Kyle Barbary, Demitri Muna, Henry Ferguson, Frédéric Grollier, Madhura M. Parikh, Prasanth H. Nair, Hans M. Unther, Christoph Deil, Julien Woillez, Simon Conseil, Roban Kramer, James E. H. Turner, Leo Singer, Ryan Fox, Benjamin A. Weaver, Victor Zabalza, Zachary I. Edwards, K. Azalee Bostroem, D. J. Burke, Andrew R. Casey, Steven M. Crawford, Nadia Dencheva, Justin Ely, Tim Jenness, Kathleen Labrie, Pey Lian Lim, Francesco Pierfederici, Andrew Pontzen, Andy Ptak, Brian Refsdal, Mathieu Servillat, and Ole Streicher. Astropy: A community Python package for astronomy. *Astron. Astrophys.*, 558:A33, October 2013. doi: 10.1051/0004-6361/201322068.
- [87] J. D. Hunter. Matplotlib: A 2d graphics environment. *Computing in Science & Engineering*, 9(3):90–95, 2007. doi: 10.1109/MCSE.2007.55.
- [88] Thomas Robitaille, Tom Rice, Chris Beaumont, Adam Ginsburg, Braden MacDonald, and Erik Rosolowsky. astrodendro: Astronomical data dendrogram creator. *Astrophysics Source Code Library*, record ascl:1907.016, July 2019.

Acknowledgements X.M. is grateful to the financial support from China Scholarships Concil. We acknowledge all the developers for their open-source codes and packages **Numpy** (84), **Scipy** (85), **Astropy** (86), **Matplotlib** (87), **Astrodendro** (88), and **FERIA** (71), which were crucial in this work.

Funding T.L. acknowledges the supports by the National Key R&D Program of China (No. 2022YFA1603100), National Natural Science Foundation of China (NSFC) through grants No.12073061 and No.12122307, and the Tianchi Talent Program of Xinjiang Uygur Autonomous Region. B.Z. acknowledges support by the Natural Science Foundation of China (NSFC,

grant No. U1831136 and U2031212) and Shanghai Astronomical Observatory (N-2020-06-09005). X.M acknowledges financial support from the program of China Scholarships Council 202304910546. G.G. and L.B. gratefully acknowledge support by the ANID BASAL project FB210003. A.H. thanks the support by the S. N. Bose National Centre for Basic Sciences under the Department of Science and Technology, Govt. of India and the CSIR-HRDG, Govt. of India for the funding of the fellowship. X.L. acknowledges support from Strategic Priority Research Program of the Chinese Academy of Sciences Grant XDB0800100. PS was partially supported by a Grant-in-Aid for Scientific Research (KAKENHI Number JP23H01221) of JSPS. E.M. acknowledges funding from the Vilho, Yrjö ja Kalle Väisälän rahasto from the Finnish Academy of Science and Letters. M.J., J.V., and D.T. acknowledge support from the Research Council of Finland grant 348342. J.-E.L. was supported by the National Research Foundation of Korea (NRF) grant funded by the Korea government (MSIT) (grant numbers 2021R1A2C1011718 and RS-2024-00416859). This research was carried out in part at the Jet Propulsion Laboratory, which is operated by the California Institute of Technology under a contract with the National Aeronautics and Space Administration (80NM0018D0004). P.G., G.G. and L.Z. are supported by Chinese Academy of Sciences South America Center for Astronomy (CASSACA) Key Research Project E52H540201. N.J.E thanks the Astronomy Department of the University of Texas for research support.

Author contributions Conceptualization: XM, TL, XL, NJE, JH, CWL, SZ, KT, SD, QZ, JEL, MJ, LZ, GG Methodology: XM, QL, TL, XC, JH, KT, QZ, XL Investigation: XM, TL, XL, XC, JH, CWL, SD, DY, SRD, QZ, JOC Visualization: XM, TL, EM, SRD Supervision: TL, GLW, CWL, MJ, XL Writing—original draft: XM, TL, XL, KTK, QL, PFG, SZ, KT, SD Writing—review & editing: XM, TL, BZ, PFG, NJE, QZ, KTK, MJ, FX, WJ, HL, PS, GG, SQ, JMV, AT, ZR, SD, SL, QL, JH, PG, AH, YZ, JEL, SZ, EM, DT, LD, LB, PrG, XT, SRD, GW, CWL, JOC, YKZ, QG, KT, GLW, ZS Validation: XM, QL, TL, ZR, SL, HL, JH, CWL, YKZ, XL, JOC, XC, PFG Formal analysis: XM, QL, TL, XC, DY, JOC Funding acquisition: TL, BZ, CWL, GLW, XL, LZ Data curation: XM, TL, SZ, WJ, FX, LZ Software: XM, TL, FX Project administration: TL, GLW Resources: CWL, BZ, GLW, DY, XL, TL

Competing interests The authors declare they have no competing interests.

Materials Availability All data needed to evaluate the conclusions in the paper are present in the paper and/or the Supplementary Materials. The ALMA data presented in this work can be found on ALMA Science Archive under project codes 2019.1.00685.S, 2021.1.00095.S, and 2021.1.00455.T. The maser data is available via <https://cdsarc.cds.unistra.fr/viz-bin/cat/J/A+A/684/A86>.

Content for supplementary materials:

Figures:

Fig. S1: Stacked image of various gas tracers

Fig. S2: The position-velocity diagrams of CCH. The elements in this figure are the same as in Fig. 8

Fig. S3: The PV diagrams of various molecules.

Fig. S4: The intensity profiles of continuum emission and different molecular line emission

Fig. S5: The moment maps of DCN and CH₃OH

Fig. S6: The χ^2 cube of the IRE fitting

Fig. S7: The moment maps and PV diagrams of CH₃CN J=12-11 K=3-5 transitions

Fig. S8: The schematic representation of the configuration of the envelope-disk system

Fig. S9: The spatial distribution of the outflow and shocked gas

Fig. S10: The channel maps of the blue lobe of CO outflow

Fig. S11: The spiral model with the highest Pearson correlation coefficient.

Fig. S12: The spectra of CO, ¹³CO, and C¹⁸O

Tables:

Table S1: The parameter range and the best-fit parameter set in the χ^2 grid search

Table S2: The outflow parameters

Table S3: The molecule species and transitions used in this study

Supplementary Material

Content:

Figures:

Fig. S1: Stacked image of various gas tracers

Fig. S2: The position-velocity diagrams of CCH. The elements in this figure are the same as in Fig. 8

Fig. S3: The PV diagrams of various molecules.

Fig. S4: The intensity profiles of continuum emission and different molecular line emission

Fig. S5: The moment maps of DCN and CH₃OH

Fig. S6: The χ^2 cube of the IRE fitting

Fig. S7: The moment maps and PV diagrams of CH₃CN J=12-11 K=3-5 transitions

Fig. S8: The schematic representation of the configuration of the envelope-disk system

Fig. S9: The spatial distribution of the outflow and shocked gas

Fig. S10: The channel maps of the blue lobe of CO outflow

Fig. S11: The spiral model with the highest Pearson correlation coefficient.

Fig. S12: The spectra of CO, ¹³CO, and C¹⁸O

Tables:

Table S1: The parameter range and the best-fit parameter set in the χ^2 grid search

Table S2: The outflow parameters

Table S3: The molecule species and transitions used in this study

Supplementary Fig. S1 presents the stacked image of H^{13}CO^+ , CCH and 3 mm continuum.

Supplementary Fig. S2 shows the PV diagrams of CCH along the selected paths.

Supplementary Fig. S3 shows the PV diagrams for DCN, H_2CO , HC_3N , SO, CH_3OH and C^{18}O cut along the major axis of the “bar”. The gas kinematics can be decomposed into two modes: the elongated and velocity-coherent structure extending beyond $4''$ and the diamond-shape structure with the clear spin-up feature. The velocity-coherent mode indicates the gas inflow along the “bar” while the “diamond” mode indicates the rotating and infalling motion at the center. The smooth transition between two modes may suggest that the gas is being transported to the central envelope and starts rotating.

Supplementary Fig. S4 presents the intensity profiles of continuum emission and different molecular line emission along the “bar”. The H^{13}CO^+ shows extended emission along the “bar” while CCH is less abundant at the center. Interestingly, despite the different angular resolution, the 3 mm continuum dust and C^{18}O in 1.3 mm observation show a similar extent, suggesting that C^{18}O is tracing a more flattened gas reservoir than DCN and 1.3 mm continuum, which is central dominant (the “nucleus”) with two shoulders and long tails (the “bar”) on both sides in the profiles.

Supplementary Fig. S5 shows the zoomed-in Moment 0 and Moment 1 maps of DCN and CH_3OH . Close to the “nucleus”, both molecular lines show tails connected to larger-scale gas streamers, as outlined by cyan dashed lines.

Supplementary Fig. S6 shows the χ^2 cube of the IRE fitting.

Supplementary Fig. S7 shows the moment maps and PV diagrams of CH_3CN $J=12-11$ $K=3-5$ transitions, which well reveal the geometry and kinematics of the pseudodisk.

Supplementary Fig. S8 is a schematic representation of the inversion of the line-of-sight velocity field between the envelope and the disk.

Supplementary Fig. S9 shows the spatial distribution of CO outflow and shocked gas traced by SiO, H_2 , masers.

Supplementary Fig. S10 shows the channel maps of ^{12}CO blueshifted high-velocity emission. The jet direction revealed in higher-velocity channels is remarkably different from the one seen in lower-velocity channels, indicating potential jet precession.

Supplementary Table S1 lists the parameter space of the χ^2 search, and the best-fit parameter set with the corresponding lowest χ^2 value.

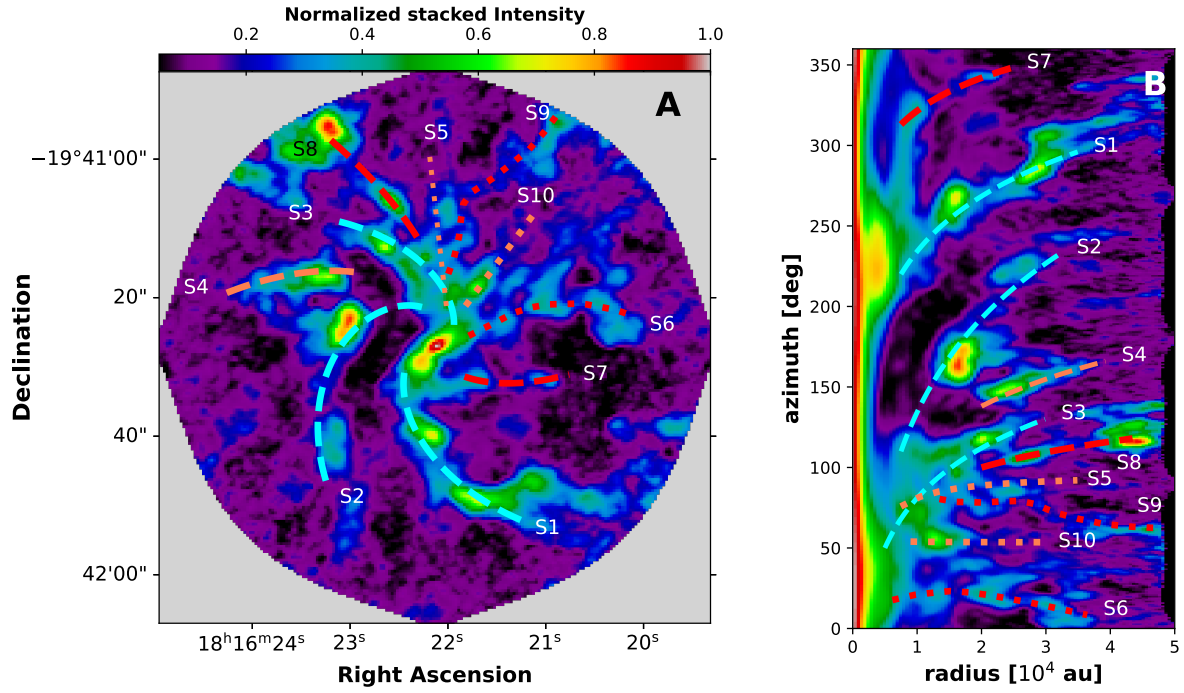
Supplementary Table S2 summarizes the calculated outflow parameters.

Supplementary Table S3 summarizes the molecule species and the transi-

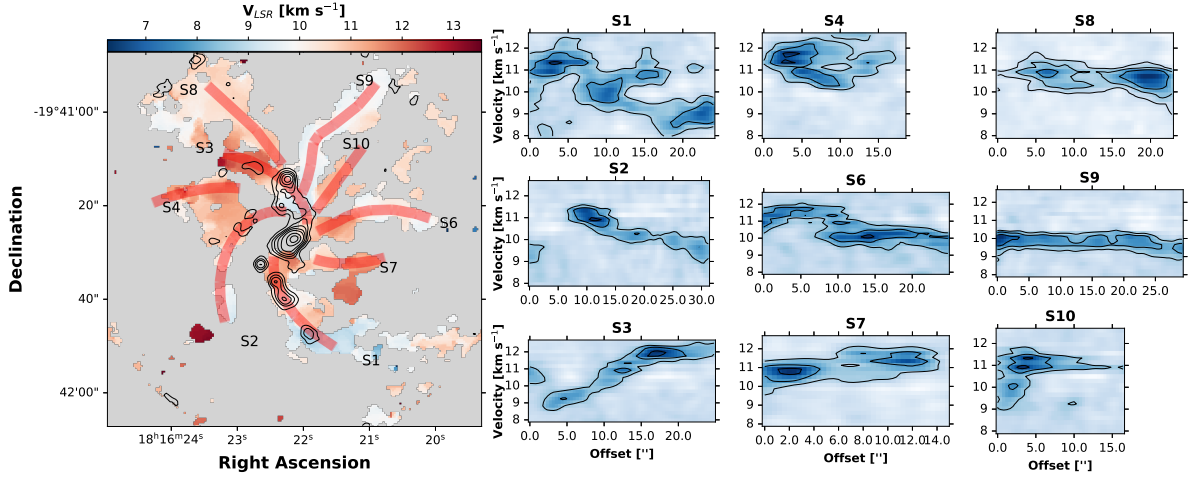
tions used in this study.

Supplementary Fig. S11 presents the best spiral model on the 3 mm continuum emission data.

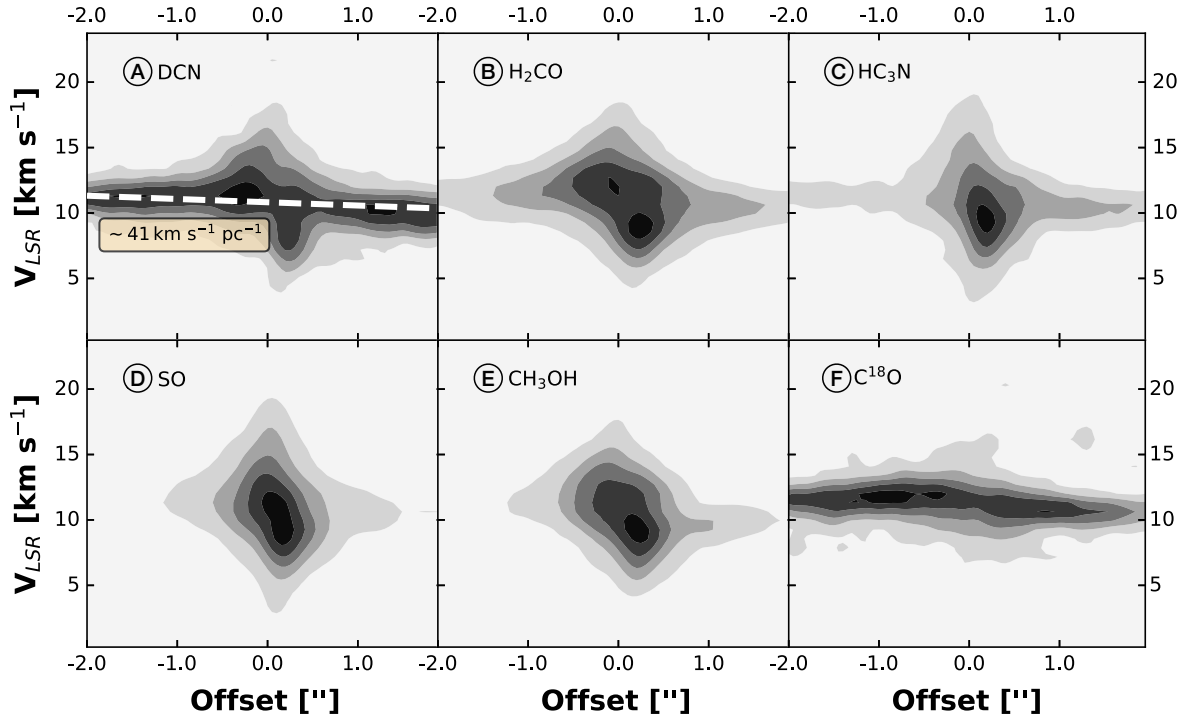
Supplementary Fig. S12 shows the spectra of ^{12}CO , ^{13}CO , and C^{18}O , and the selected velocity ranges for outflow.



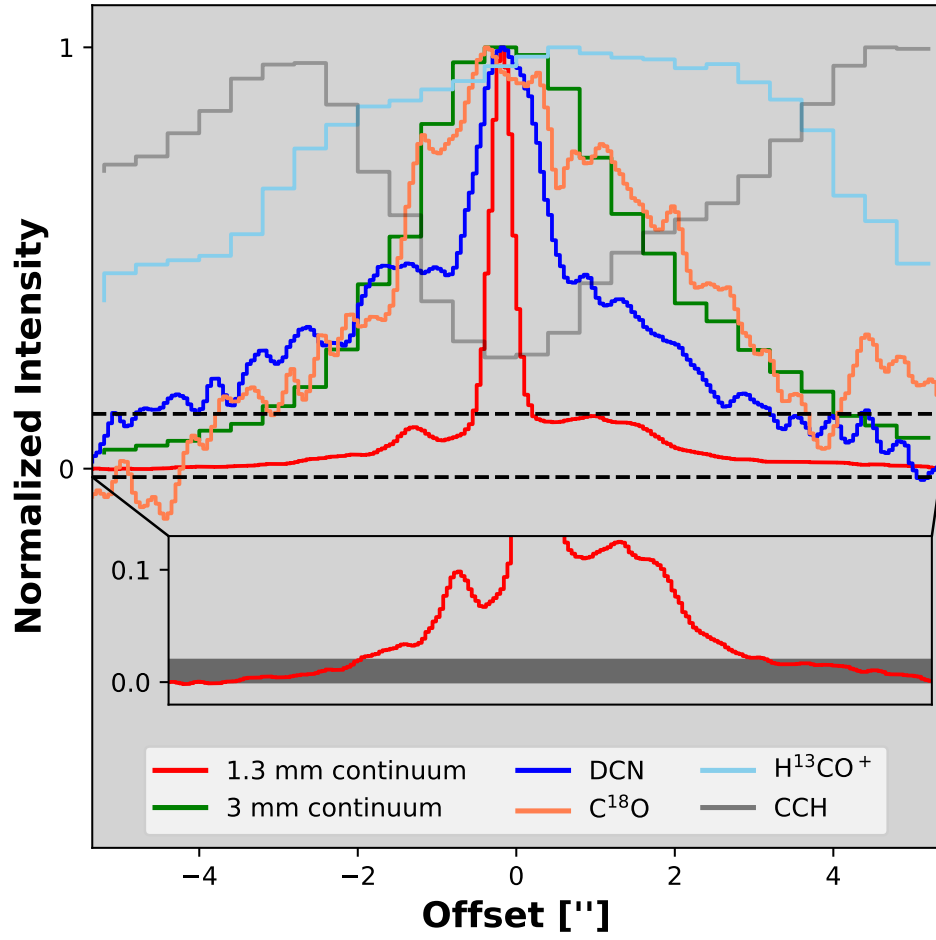
Supplementary Fig. 1 | The overall gas distribution reveals an intricate spiral-like hub-filament system. Panel A shows the stacked image of H^{13}CO^+ , CCH and 3 mm continuum after normalization while **panel B** shows the polar projection of **panel A**. The cyan, orange, and red curves outline the filaments identified in 3 mm continuum, H^{13}CO^+ , and CCH in Fig. 6 and 7.



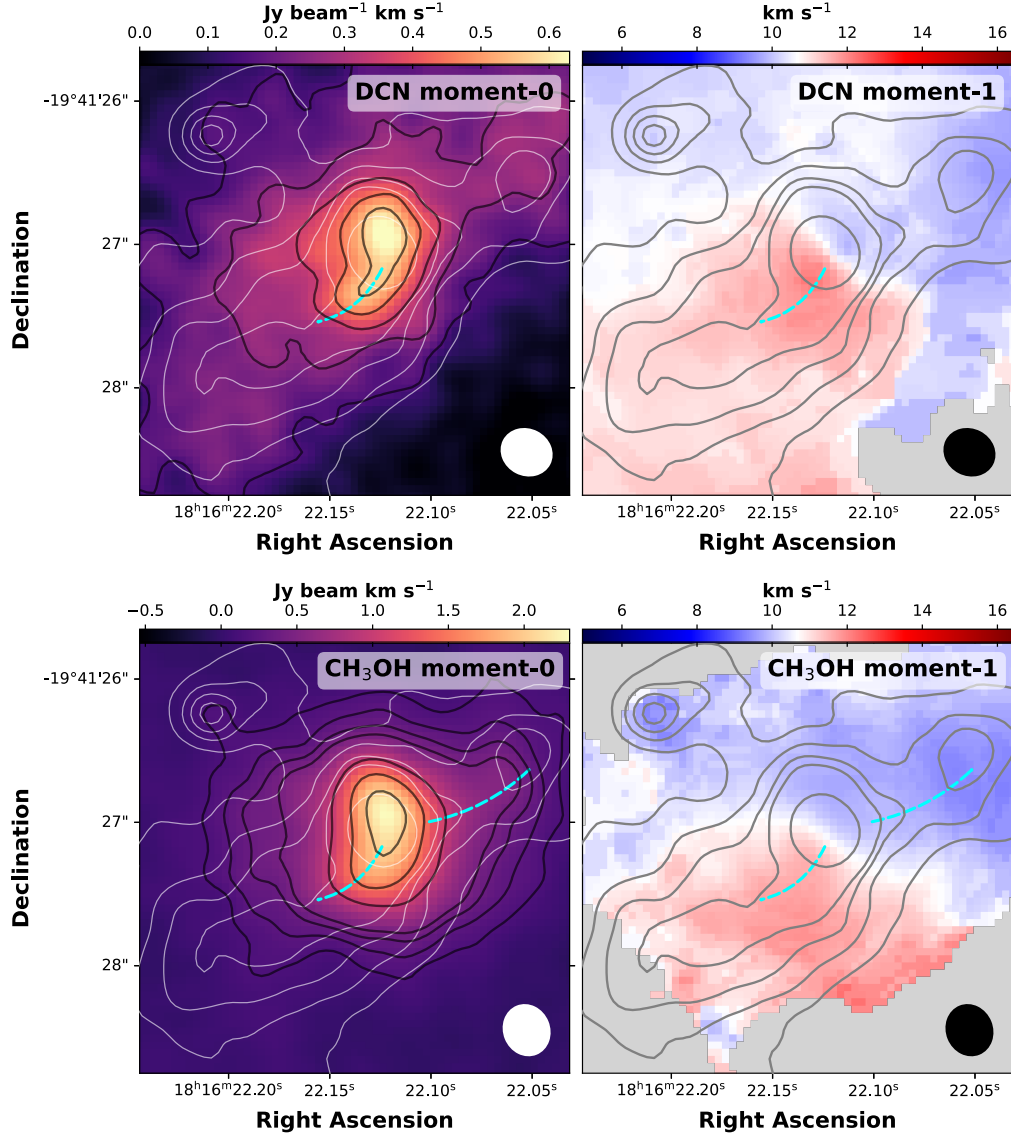
Supplementary Fig. 2 | The velocity coherent filaments traced by CCH. Same as in Fig. 8.



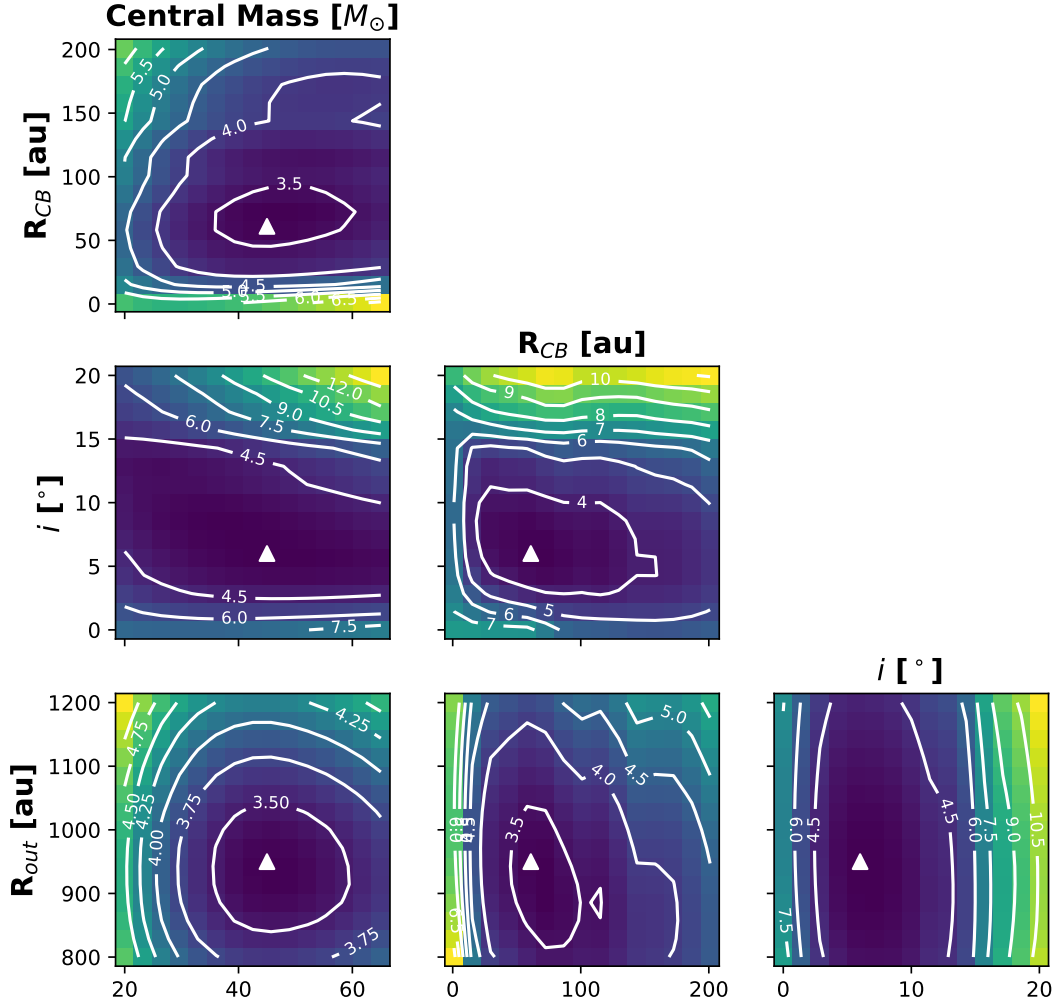
Supplementary Fig. 3 | The kinematics of the streamer-envelope system. The position-velocity diagrams of different molecules (marked in the upper left corner of each panel) along the same cut are plotted as filled contours. All the contours start from 10% of the peak intensity and increase on 20% steps. The direction of the PV cut is labeled as the green dashed line in Fig. 2b but for the inner 4". The white dashed lines in panel A represent the global velocity gradient along the “bar” of $\sim 41 \text{ km s}^{-1} \text{ pc}^{-1}$.



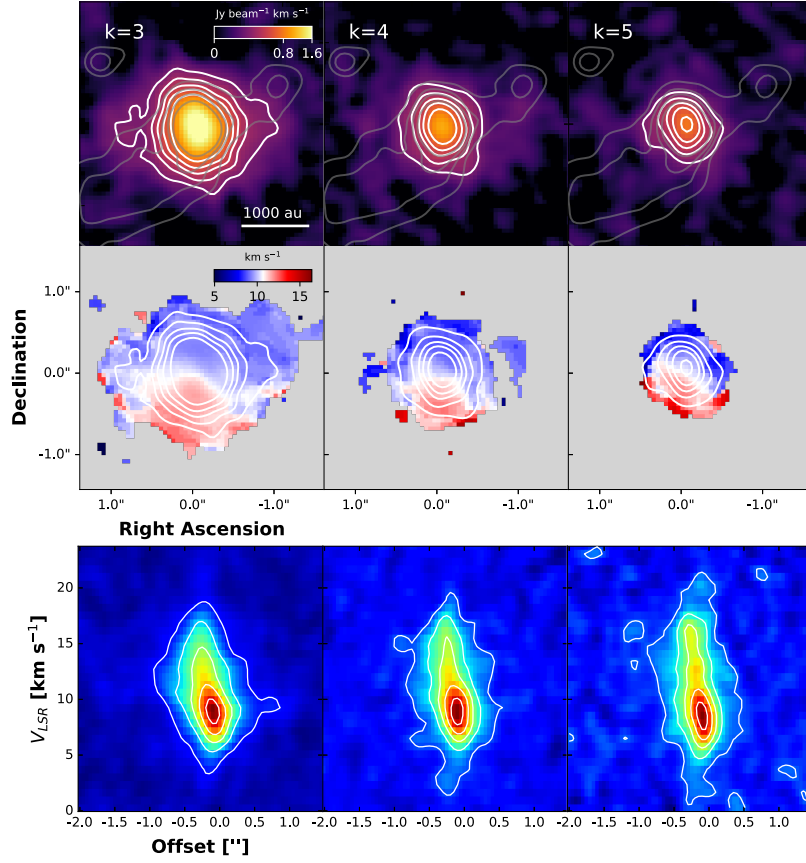
Supplementary Fig. 4 | The normalized intensity profile of the continuum maps and different molecules along the major axis of the bar. The dashed horizontal lines mark the zoom-in range. The grey band in the zoom-in axis represents the $3\text{-}\sigma_{1.3\text{mm}}$.



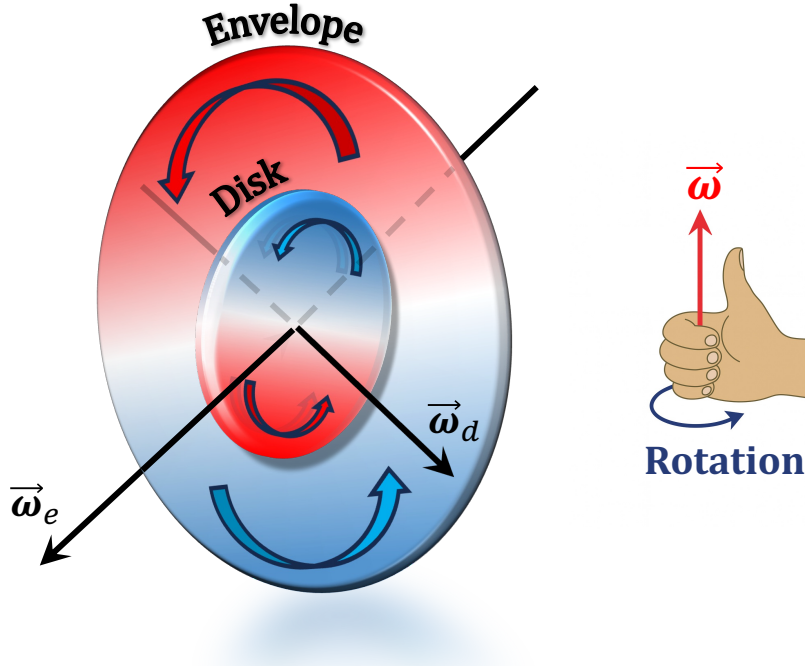
Supplementary Fig. 5 | The integrated intensity and intensity-weighted velocity maps of DCN and CH₃OH. This figure shows the zoom-in view of the integrated intensity (**left**) and centroid velocity (**right**) of DCN (**top**) and CH₃OH (**bottom**). The 1.3 mm continuum emission is shown as the white contours in the left column and grey contours in the right column. The black contours in the upper left panel are the integrated intensity of DCN at $[3, 5, 7, 9, 11] \times 0.05 \text{ Jy beam}^{-1} \text{ km s}^{-1}$. The black contours in the lower left panel are the integrated intensity of CH₃OH at $[3, 5, 7, 9, 20, 30, 40] \times 0.05 \text{ Jy beam}^{-1} \text{ km s}^{-1}$. The cyan dashed curves trace the ‘tails’ — the terminal end of the converging streamers. The synthesized beam is shown at the lower right corners.



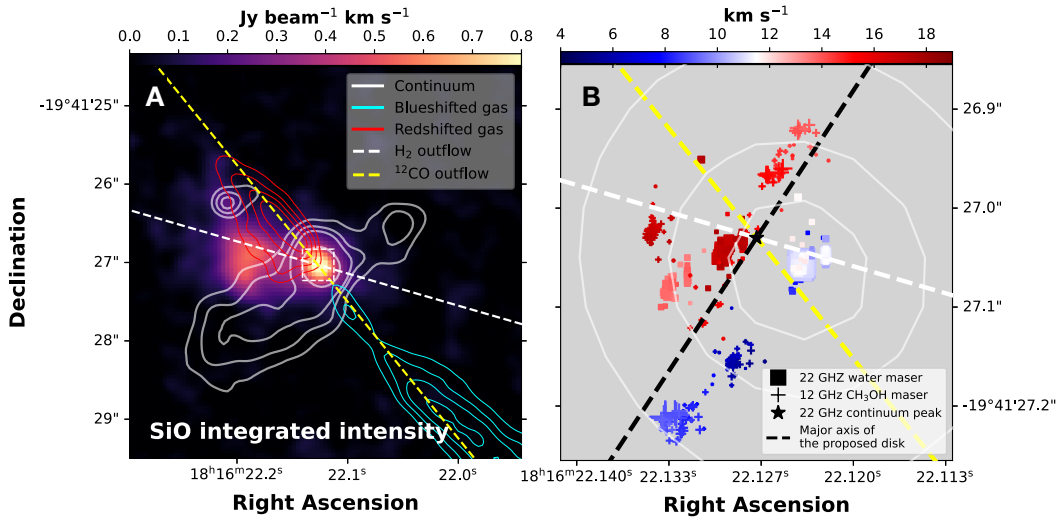
Supplementary Fig. 6 | χ^2 grid search performed in $\text{CH}_3\text{OH } 4_2 - 3_1 \text{ E1 } vt = 0$. These colormaps represent the slices of the χ^2 cube across the best-fit parameter set marked by the white triangles. The parameter ranges are summarized in table S1.



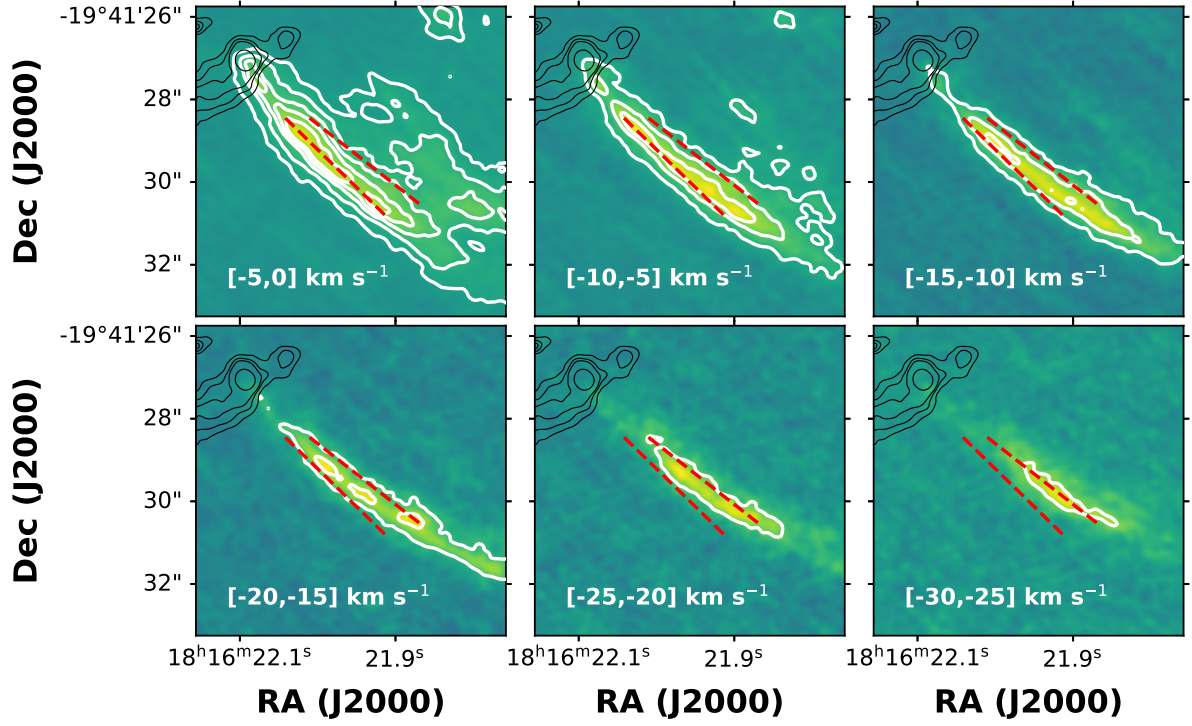
Supplementary Fig. 7 | Moment maps and PV diagrams of CH_3CN J=12-11 K=3-5. The top and middle rows are their integrated intensity maps and centroid velocity maps, respectively, and the bottom row is their PV diagrams. The white contours in the top and middle rows are at $[3,5,7,9,12] \times 0.06 \text{ Jy beam}^{-1} \text{ km s}^{-1}$. The gray contours in the top rows are 1.3 mm continuum emission at $[10,15,20,30] \times \sigma_{1.3\text{mm}}$. The white contours in the bottom rows are at 10%, 30%, 50%, 70%, 90% of the peak intensities.



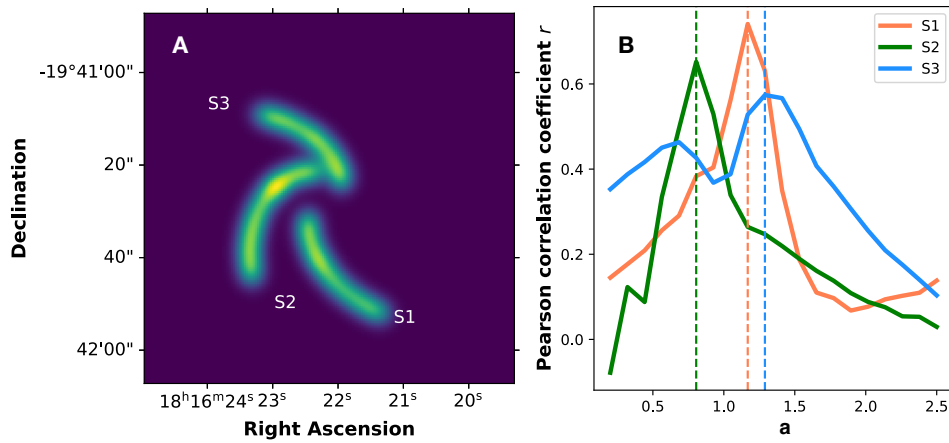
Supplementary Fig. 8 | Schematic representation of inclination difference of the envelope-disk system. Vectors $\vec{\omega}_e$ and $\vec{\omega}_d$ denote the angular momentum vectors of the envelope and the disk, respectively. The rotation of both the envelope and disk follows the right-hand rule.



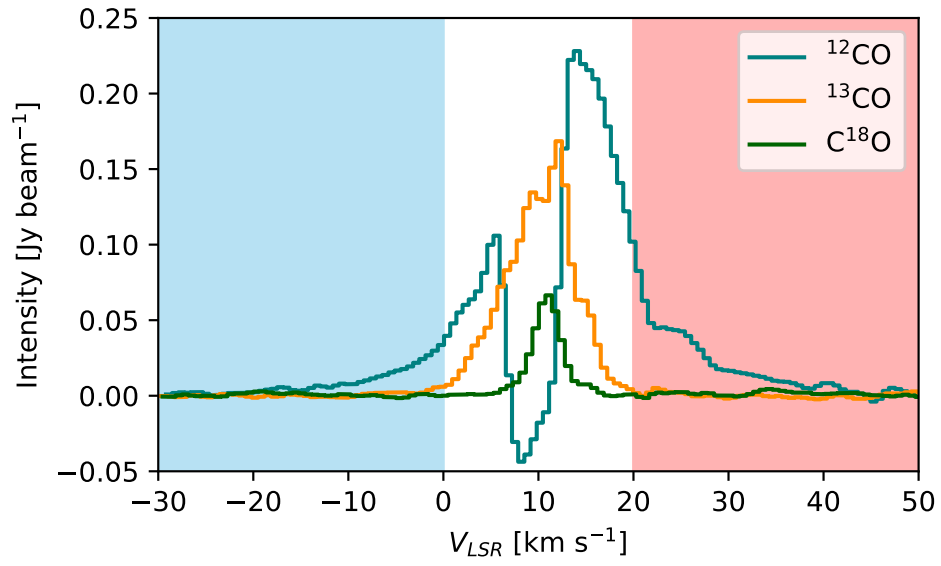
Supplementary Fig. 9 | Misalignment between outflow gas traced by ¹²CO and the shocked gas traced by SiO, H₂ and 22 GHz water masers. **A**, the background shows the SiO integrated intensity. The redshifted and blueshifted outflow gas traced by ¹²CO are shown as red and cyan contours respectively, and the white contours are the 1.3 mm continuum emission. The red and cyan contours are at the level of $[7, 9, 11, 13] \times \sigma_{12\text{CO}}$ where $\sigma_{12\text{CO}} = 0.12 \text{ Jy beam}^{-1} \text{ km s}^{-1}$. Contours of the continuum emission are at the level of $[15, 19, 30, 50, 80, 150] \times \sigma_{1.3\text{mm}}$ to discard the diffuse emission and emphasize the dusty streamer. The white dashed line represents the direction of H₂ knots (25, 65). The dashed square at the center of the image shows the view of panel B. **B**, Maser distribution inside the innermost 400 au region. The square and plus symbols mark the 22 GHz water masers and the 12 GHz methanol masers, respectively. The white dashed line is the same as in panel a. The black dashed line represents the major axis of the proposed disk.



Supplementary Fig. 10 | The ^{12}CO integrated intensity maps of the blue lobe over every 5 km s^{-1} from -30 to 0 km s^{-1} . The background and white contours are for the ^{12}CO integrated intensity at $[10, 20, 30, 40, 50] \times \sigma_{^{12}\text{CO}}$, where $\sigma_{^{12}\text{CO}} = 12 \text{ mJy beam}^{-1} \text{ km s}^{-1}$. The black contours mark the 1.3 mm continuum emission at $[9, 13, 17, 50] \times \sigma_{1.3\text{mm}}$. The two red dashed lines outline the jet direction in low- and high-velocity channels.



Supplementary Fig. 11 | **A**, the best-match spiral model. **B**, the Pearson correlation coefficient r of the growth rate a ranging from 0.2 to 2.5 .



Supplementary Fig. 12 | The spectra of ^{12}CO , ^{13}CO , and C^{18}O at the 1.3 mm continuum peak position. Different molecules are labeled as in the legend. The blue-shaded and red-shaded areas are the selected velocity ranges for blueshifted and redshifted lobes.

Supplementary Table 1 | Free parameters and the best-fit parameter set in the χ^2 grid search for CH₃OH

Parameters	Range	Best value	Reduced χ^2
$M [M_\odot]$	20–70	45	3.4
$i [^\circ]$	0–20	6	
$r_{\text{CB}} [\text{au}]$	0–200	60	
$r_{\text{out}} [\text{au}]$	800–1200	950	

Supplementary Table 2 | Outflow parameters of I18134-1942

Lobe	Δv km s ⁻¹	λ_{max} 10 ⁻³ pc	t_{dyn} 10 ³ yr	P_{out} 10 ⁻¹ M_\odot km s ⁻¹	F_{out} 10 ⁻³ M_\odot km s ⁻¹ yr ⁻¹	\dot{M}_{w} 10 ⁻⁷ M_\odot yr ⁻¹
Blue	[-30,0]	49.91	1.11	3.16	2.85	5.70
Red	[20,50]	18.41	0.41	0.73	1.79	3.59

Supplementary Table 3 | The molecule species and transitions used in this study

Species		Rest Frequency (GHz)	E_u (K)
3 mm			
H ¹³ CO ⁺	$J = 1 - 0$	86.754288	4.16
CCH	$N_{J,K} = 1_{3/2,2} - 0_{1/2,1}$	87.316898	4.19
1.3 mm			
SiO	$J = 5 - 4$	217.10498	31.26
H ₂ CO	3(0, 3)-2(0, 2)	218.222192	20.96
DCN	$J = 3 - 2$	217.238538	20.85
HC ₃ N	$J = 24 - 23$	218.324723	130.98
CH ₃ OH	$4_2 - 3_1$ $E1$ $vt = 0$	218.440063	45.46
CH ₃ CN	$J = 12 - 11, K = 3$	220.7090165	133.16
	$J = 12 - 11, K = 4$	220.6792869	183.15
	$J = 12 - 11, K = 5$	220.6410839	247.40
C ¹⁸ O	$J = 2 - 1$	219.560354	15.81
SO	6(5)-5(4)	219.949442	34.98
¹² CO	$J = 2 - 1$	230.538	16.59